

---

# Synchrotron Small-Angle X-Ray Scattering and Small-Angle Neutron Scattering Studies of Nanomaterials

# 13

Hiroyuki Takeno

## Contents

1	Definition of the Topic .....	717
2	Overview .....	718
3	Introduction .....	718
4	Experimental and Instrumental Methodology .....	720
5	Key Research Findings .....	722
5.1	Hierarchical Structures of Various Soft Materials .....	722
5.2	Structural Analysis of Soft Materials .....	724
5.3	Contrast-Matching and Contrast Variation Methods in SANS and SAXS .....	736
5.4	Time-Resolved Scattering Measurements .....	745
5.5	Complementary Utilization of SAXS and SANS .....	748
6	Conclusions and Future Perspective .....	750
	References .....	751

---

## 1 Definition of the Topic

Small-angle scattering is a very powerful technique to probe structures of materials. X-ray, neutron, and light scattering techniques present structural information of materials in a wide range from nanometer to micrometer scale. Chemists, physicists, and engineers have used these techniques to study structures of various systems from hard to soft materials. In this topic, we focus upon soft materials such as polymers, gels, colloids, etc. We present a review of their recent studies with small-angle X-ray scattering (SAXS) and small-angle neutron scattering (SANS).

---

H. Takeno (✉)

Department of Chemistry and Chemical Biology, School of Science and Technology, Gunma University, Kiryu, Gunma, Japan

e-mail: [takeno@gunma-u.ac.jp](mailto:takeno@gunma-u.ac.jp)

---

## 2 Overview

In a typical experimental setup, synchrotron SAXS and SANS are capable of probing structures of aggregates in the range of 1–100 nm. The use of ultra-small-angle scattering techniques such as ultra-small-angle X-ray scattering (USAXS) and ultra-small-angle neutron scattering (USANS) makes it possible to probe structures of aggregates with larger size on a micrometer scale. Here we review some structural studies on various soft materials, which form a hierarchical organization. Recent development of synchrotron radiation source and neutron facility allows us to obtain scattering data on various length scales. It is shown that combination of various scattering methods provides us with information on hierarchical structures of soft materials from a microscopic to macroscopic level. The structural analysis on each level is also presented in the text. Furthermore, contrast variation and contrast-matching SAXS and SANS methods are very effective for structural investigation of multicomponent nanomaterials, e.g., these methods are very useful to probe internal structures of complex systems such as polymer micelles, polymer–inorganic nanocomposite gels, and rubber-filler systems swollen in an organic solvent.

---

## 3 Introduction

So far, many good books regarding experimental techniques and structural analysis by small-angle scattering have been published [1–6]. General data treatments, instrumentations, and data analysis by small-angle X-ray scattering (SAXS) are abundantly described by famous books of Guinier and Fournet [1], Glatter and Kratky [2], and Feigin and Svergun [3]. The book written by Higgins and Benoit presents a comprehensive data analysis of small-angle neutron scattering (SANS) in polymeric systems [4]. These books have provided many researchers with fundamentals of scattering techniques. Also, it is important to learn how their techniques could be used in practice. Recent development of brilliant X-ray sources and neutron facilities is striking, and there are progress and improvements in synchrotron X-ray and neutron scattering instruments. Thus, in this book chapter we introduce updated studies of soft materials with X-ray and neutron scattering. Recently, importance of SANS and SAXS is increasing more and more in the field of soft material science. As a matter of fact, in the past decade, there have been published a large number of review articles regarding SANS and SAXS studies of various soft materials such as copolymers, polymer blends, branched polymers [7], starch [8, 9], polyelectrolyte systems [10], polymer latexes [11], polymer gels [12], protein and peptide self-assembled materials [13], and three-dimensional periodic complex systems [14].

Though both SANS and SAXS have played an important role in probing structures of nanomaterials, each of the SAXS and SANS techniques has unique characteristics. The X-ray scattering is caused mainly by interactions of the incident beam with electrons, while the neutron scattering is done by those of the incident beam with nucleus [3]. As a consequence, the X-ray scattering from atoms increases with the increase of atomic number and has a scattering angle dependence, since

**Table 13.1** Scattering length  $b$  of some elements for X-ray and neutron scattering [3, 15]

Element	$b$ for X-ray ( $10^{-12}$ cm)	$b$ for neutron ( $10^{-12}$ cm)
H	0.282	-0.374
D	0.282	0.667
C	1.69	0.665
N	1.97	0.94
O	2.26	0.58
S	4.51	0.28
Na	3.10	0.36
Cl	4.79	0.96

distribution of electrons spreads around nuclei. The absorption of X-rays also increases with the atomic number and the wavelength. On the other hand, neutron scattering from atoms is independent of the scattering angle due to the fact that dimensions of nucleus are much smaller in comparison with that of the neutron wavelength and does not have a definite relationship with the atomic number. The scattering length (or amplitude)  $b$  of main elements in soft materials for X-ray and neutron scattering is listed in Table 13.1. Note that the scattering intensity is proportional to the square of the scattering length. In neutron scattering, there are large differences between scattering lengths of hydrogen (H) and deuterium (D). Deuterium labeling is often utilized in neutron scattering experiments in order to change the scattering contrast.

Characteristics of synchrotron SAXS and SANS are compared in the following.

### Synchrotron X-Rays

- (i) Heavier atoms have larger scattering length.
- (ii) The beam size is usually very small due to high photon fluxes (typically submillimeter), which enables us to obtain precise data with a very small amount of samples.
- (iii) Energetic and angular resolutions are high.

### Neutrons

- (i) Spatial information on light atoms such as hydrogen can be evaluated.
- (ii) Larger beam size in comparison with synchrotron X-rays is used (typically 5–10 mm).
- (iii) Information on magnetic structures of condensed matter can be obtained from the magnetic scattering.
- (iv) Contrast variation and contrast-matching techniques are very effective to probe the structure of complicated systems. Especially, in aqueous solutions and/or hydrogels, we can easily change scattering contrast by preparing  $\text{H}_2\text{O}/\text{D}_2\text{O}$  with different mixing ratios.

In the past two decades, high-performance materials have attracted material scientist's interest due to the potential applications in various fields. In many cases, functionality of materials is closely related to the internal structure. With the

high performance of materials, the system has grown more complex, and therefore, it is important to clarify the structure of the complicated system in the modern material science. We will show that combination of various scattering methods and contrast variation methods are useful to analyze structures of the complicated systems.

This book chapter deals with structural studies of complex soft materials such as polymeric systems, self-assembling systems, composite systems, etc. using X-ray and neutron scattering. Constitution of this book chapter is as follows: Sect. 4 briefly describes a fundamental of scattering methods. In Sects. 5.1 and 5.2, we briefly present an overview of scattering behaviors of hierarchically organized structures on each level. These are common to both of X-ray and neutron scattering. In Sect. 5.3, recent structural studies of soft materials using contrast variation SAXS and SANS are reviewed. Although the contrast variation method has been utilized from old times, recently, it largely has displayed the power against structural analysis of various complex materials. In Sects. 5.4 and 5.5, we introduce structural evolution using time-resolved scattering measurements and complementary use of X-ray scattering and neutron scattering. Complementary use of neutron and X-ray scattering may be effective in the structural studies of various complex materials [16, 17].

## 4 Experimental and Instrumental Methodology

We show a schematic representation of typical small-angle scattering experiments in Fig. 13.1. In the synchrotron small-angle X-ray and neutron scattering experiments, the scattered intensity is usually measured with a two-dimensional detector such as CCD, imaging plate, and PILATUS. Therefore, we can obtain information about anisotropic structures of condensed matters [18–20], and the measurements are often performed under external fields, e.g., mechanical, electric, and magnetic fields.

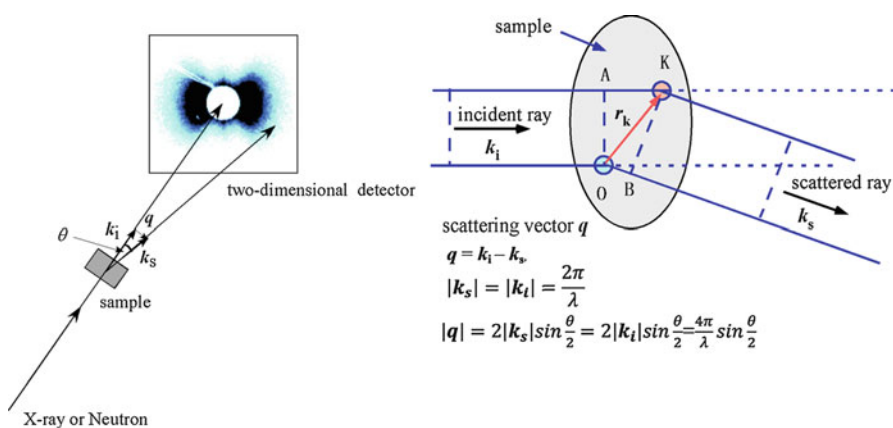


**Fig. 13.1** A schematic diagram of a typical synchrotron small-angle X-ray or neutron scattering experiments and definition of scattering vector  $q$

When an incident ray is scattered by particles located at positions of O and K, the path length difference between two scattered rays is presented by

$$AK - OB = \left( \mathbf{r}_k \cdot \frac{\mathbf{k}_i}{k_i} \right) - \left( \mathbf{r}_k \cdot \frac{\mathbf{k}_s}{k_s} \right), \quad (13.1)$$

and therefore, the phase difference  $\phi_k$  is described by

$$\phi_k = \left( \frac{2\pi}{\lambda} \right) \left( \mathbf{r}_k \cdot \frac{\mathbf{k}_i - \mathbf{k}_s}{k} \right) = (\mathbf{r}_k \cdot \mathbf{q}), \quad (13.2)$$

where  $\mathbf{k}_i$  and  $\mathbf{k}_s$  are wavevectors of incident ray and scattered ray and the magnitudes are  $k_i = k_s = k = \frac{2\pi}{\lambda}$ . The scattering data are analyzed with scattering vector  $\mathbf{q}$  defined by  $\mathbf{q} = \mathbf{k}_i - \mathbf{k}_s$ . The magnitude of the scattering vector is expressed by

$$q = 4\pi \frac{\sin(\theta/2)}{\lambda}, \quad (13.3)$$

where  $\theta$  and  $\lambda$  represent the scattering angle and wavelength, respectively. The amplitude of the scattered wave at point K can be described by

$$A_k = A_0 b e^{-i(\omega t + \phi_k)} = A_0 b e^{-i(\omega t + \mathbf{r}_k \cdot \mathbf{q})}, \quad (13.4)$$

where  $A_0$  is the amplitude of the incident wave and  $b$  is the scattering length. We can generalize Eq. (13.4) for the system composed of many identical scatterers, i.e., the total contribution  $A_t$  is described as follows:

$$A_t = \sum_k A_0 b e^{-i(\omega t + \mathbf{r}_k \cdot \mathbf{q})} = A_0 e^{-i\omega t} \sum_k b e^{-i\mathbf{r}_k \cdot \mathbf{q}}. \quad (13.5)$$

Thus, the scattering amplitude  $F(q)$  is defined by

$$F(q) = \sum_k b e^{-i\mathbf{r}_k \cdot \mathbf{q}}, \quad (13.6)$$

and the scattering intensity is presented by

$$I(q) = F(q) \cdot F(q)^*. \quad (13.7)$$

When the scatterers are continuously distributed in a sample,  $F(q)$  can be replaced by the following integral form:

$$F(q) = b \int n(r) e^{-i\mathbf{r} \cdot \mathbf{q}} d\mathbf{r} \quad (13.8)$$

$n(r)$  is the local density of the scatterer at a point  $r$ . The relationship between the length scale of a structure in real space  $\Lambda$  and  $q$  is presented in the following form:

$$\Lambda = \frac{2\pi}{q}. \quad (13.9)$$

The data collection, data reduction, and data correction in SAXS experiments were recently written in details by a review article of Pauw [21, 22]. In a similar manner, reduction and correction of SANS data are conducted. Software tools for small-angle scattering data analysis are also important [23–25]. A lot of software packages to analyze small-angle scattering data can be found at the SAS portal (URL: <http://smallangle.org>).

---

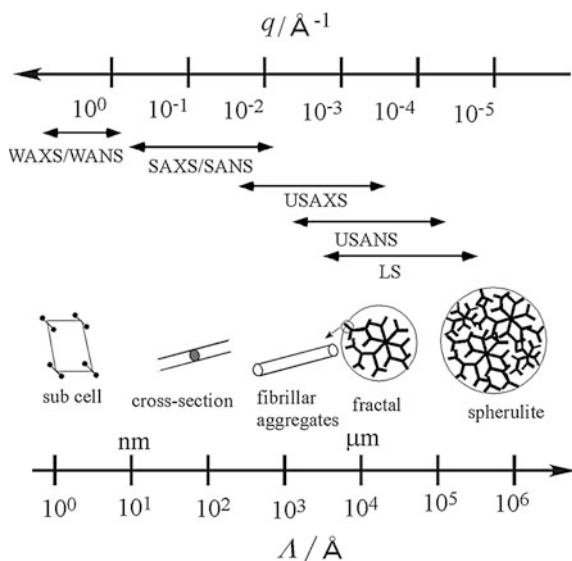
## 5 Key Research Findings

In the following sections, we will review recent structural studies of soft materials investigated by combination of various scattering methods and by using a sophisticated analysis such as contrast variation SANS and SAXS methods and will show scattering functions from particles with various structural morphologies. Here although we introduce structural studies on polymer–nanoparticle composite gel, polymer micelles, and organogel comprising low molecular weight organogelator (LMOG), the analysis can be applied to other similar systems.

### 5.1 Hierarchical Structures of Various Soft Materials

Recently, facilities of synchrotron radiation and neutron sources around the world are remarkably developing. Combination of various scattering methods allows us to obtain structural information in a broad  $q$  range. Nowadays, simultaneous SAXS and wide-angle X-ray scattering (WAXS) measurements can be performed in many synchrotron beamlines over the world [26–30]. Ultra-small-angle X-ray scattering (USAXS), ultra-small-angle neutron scattering (USANS), and very-small-angle neutron scattering (VSANS) are used to extend scattering data in a very low  $q$  range, i.e., structural information on larger length scales. Conventional Bonse–Hart type of USAXS and USANS techniques had been limited to samples with high contrast and resolved only in one dimension [31, 32]. Therefore, they were not appropriate for measurements of anisotropic samples. However, development of recent USAXS/USANS instruments such as developed Bonse–Hart configuration using multiple reflection and a pinhole USAXS at very long camera length in synchrotron sources facilitates utilization of various soft materials [33–40]. Such instrumental improvement allows us to obtain two-dimensional scattering data and to probe structures of samples with low scattering contrast [18, 36, 41, 42]. USAXS studies in polymeric systems such as polymer gels, polymer solutions, polymer

**Fig. 13.2** Hierarchical structures of low molecular weight organogel and length scale covered in various scattering methods



blends, polymer nanocomposites, colloidal gels, and rubber-filler systems can be found in review articles of Zhang and Ilavsky and Takenaka [42, 43].

As mentioned above, combining various scattering techniques makes it possible to obtain structural information of a broad length scale ranging from nanometers to micrometers [43]. Combination of these methods is useful to investigate hierarchical structures of soft matters on multilevels as shown in Fig. 13.2.

Here let us show a scattering profile combined by various scattering methods for an organogel composed of a LMOG, which entraps various organic solvents by self-assembly of the gelator molecules at very low concentrations [44, 45]. The self-assembly forms a fibrillar network, so that the solvents are immobilized. The self-assembled structure of a typical organogel is shown in Fig. 13.3. The graph depicts a scattering profile of 7 wt% 12-hydroxystearic acid (12-HSA)/toluene gel obtained by combining various scattering methods such as SAXS, SANS, focusing SANS [37, 38], and light scattering (LS). The profile shows that the structure caused by self-assembly of the LMOG molecules forms a hierarchical organization at various levels. The peaks at  $q = 0.13$  and  $0.38 \text{ \AA}^{-1}$  correspond to (001) and (003) peaks, respectively, which correspond to reflections from a long spacing of the long-chain fatty acids. The peak position is located in the same position as that of crystalline powder without any solvents [46, 47].

A shoulder peak at  $q \sim 0.046 \text{ \AA}^{-1}$  originates from cross-sectional scattering of fibrillar aggregates. The peak position suggests that the organogel is composed of nanofibers with a cross section of the radius of 8 nm with a comparatively narrow size distribution [48]. The scattering function from fibrillar aggregates (rod particles) exhibits a power law of  $q^{-1}$  in a small  $q$  range as shown in details later [2]. The scattering behavior of the organogel has an exponent of  $-1.2$  larger than the absolute value of  $-1$  in the small  $q$  range, which may suggest branching of fibrillar

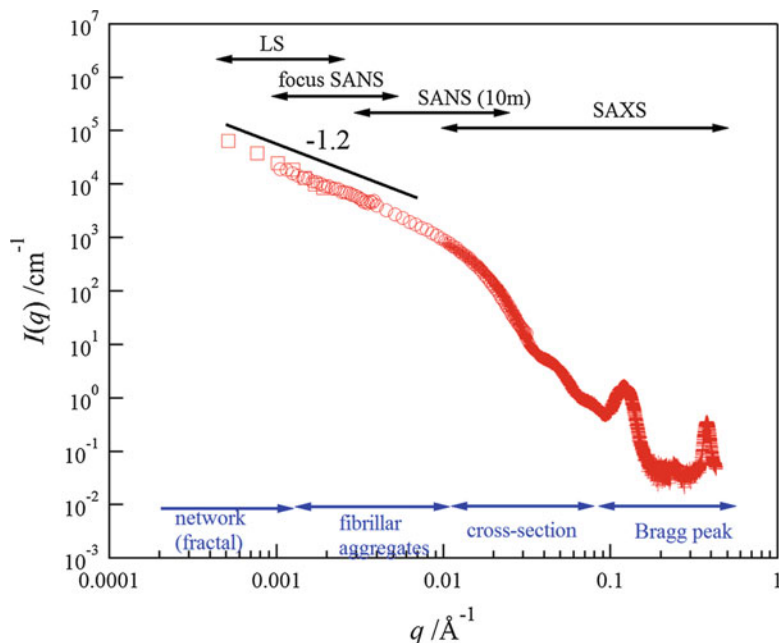


**Fig. 13.3** A scattering profile of a low molecular weight organogel obtained by combining various scattering methods (*SAXS*, *SANS*, *focusing SANS*, and *LS*)

aggregates. The power-law scattering behavior in the small  $q$  range suggests that the network structure may exhibit a fractal nature [49, 50]. The schematic illustration of the hierarchical structures predicted from various scattering data is shown in Fig. 13.2. Various soft material systems other than LMOG also form hierarchical organization. Hierarchical structures of rubber-filler (carbon black or silica particles) systems were studied in depth by Takenaka et al. [43, 51–53]. They demonstrated by using combined scattering methods that the structures consist of multilevel structures such as (i) surface of primary particles, (ii) primary particles, (iii) aggregates composed of several fused primary particles, and (iv) mass-fractal agglomerate [51]. The combined scattering techniques are also effective for phase-separated polymer blends [54], colloidal silica and carbon [55], polymer electrolyte membranes [56], ceramics [57], spongelike polymer gels [58], clay suspension [59, 60], and cellulose synthesized via enzymatic polymerization [61, 62].

## 5.2 Structural Analysis of Soft Materials

Analysis of scattering data obtained by combination of various scattering methods is important. Here we shall show theoretical scattering function on each level and the unified approach to small-angle scattering of the multilevel structures such as the Beaucage model [63–66], which has been often used for analysis of multilevel



structures [67–69]. Scattering models for the multilevel structures other than the Beaucage model have been proposed by some researchers [70, 71]. In the following section, we shall briefly describe outline of these structural analyses.

### 5.2.1 Spherical Particles

The scattering intensity for spherical monodisperse particles can be written by

$$I(q) = n_p V_p^2 \Delta\rho^2 P(q) S(q), \quad (13.10)$$

where  $n_p$  and  $V_p^2$  represent the number density of the particles and the square of the volume, respectively.  $\Delta\rho$  is the scattering length density.  $P(q)$  and  $S(q)$  are the form factor of the particles and the structure factor. The former comes from the intra-particle interferences, while the latter comes from the interparticle interferences. In dilute systems the interactions between the particles can be ignored, and therefore,  $S(q)$  approaches unity.

Series expansion of  $P(q)$  in a small  $q$  range ( $qR_g \ll 1$ ) leads to Guinier's law,

$$P(q) \cong P(0) \exp\left(-\frac{1}{3} R_g^2 q^2\right), \quad (13.11)$$

where  $R_g$  is the radius of gyration of a particle. Guinier's law is applicable to particulate systems with an arbitrary shape other than spherical particles. We can estimate  $R_g$  from the plot of  $\ln(I(q))$  vs.  $q^2$  for dilute systems.  $R_g$  of objects with various shapes is summarized in Table 13.2.

In the intermediate  $q$  range,  $P(q)$  depends upon the size and the shape of the particles.  $P(q)$  of spherical particles with radius  $R$  is presented by

$$P(q) = \left[ \frac{3\{\sin(qR) - qR \cos(qR)\}}{(qR)^3} \right]^2. \quad (13.12)$$

**Table 13.2**  $R_g$  of objects with various geometrical shapes

Sphere with radius $R$	$R_g = \left(\frac{3}{5}\right)^{1/2} R$
Spherical shell with radius $R_1 > R_2$	$R_g = \left(\frac{3}{5} \frac{R_1^5 - R_2^5}{R_1^3 - R_2^3}\right)^{1/2}$
Rectangular parallelepiped (sides $2a, 2b, 2c$ )	$R_g = \left(\frac{a^2 + b^2 + c^2}{3}\right)^{1/2}$
Cylinder (half-length $H$ , radius $R$ )	$R_g = \left(\frac{R^2}{2} + \frac{H^2}{3}\right)^{1/2}$
Ellipsoid (half axis $a, b, c$ )	$R_g = \left(\frac{a^2 + b^2 + c^2}{5}\right)^{1/2}$

Taking into consideration the size distribution of the radius, the scattering intensity is expressed by

$$I(q) = \int_0^{\infty} (\Delta\rho)^2 V_p^2 N(R) P(q) dR, \quad (13.13)$$

where  $N(R)$  represents the distribution function of the radius, and the lognormal distribution or the Gaussian distribution is often used.

$$N(R) = n_p \left( \frac{1}{R\sqrt{2\pi\ln\sigma}} \right) \exp \left[ -\frac{(\ln R - \ln R_0)^2}{2\ln^2\sigma} \right] \quad (13.14)$$

or

$$N(R) = n_p \left( \frac{1}{\sqrt{2\pi}\sigma} \right) \exp \left[ -\frac{(R - R_0)^2}{(2\sigma^2)} \right] \quad (13.15)$$

$R_0$  and  $\sigma$  are the geometric mean and the geometric standard deviation of the distribution, respectively.

### 5.2.2 Nonspherical Particles

For nonspherical monodisperse systems, the scattering intensity can be written by [72]

$$I(q) = n_p V_p^2 \Delta\rho^2 P(q) S_{\text{app}}(q) \quad (13.16)$$

with

$$S_{\text{app}}(q) = 1 + \frac{|\langle F(q) \rangle|^2}{P(q)} [S(q) - 1]. \quad (13.17)$$

Here the bracket in  $|\langle F(q) \rangle|^2$  is an average weighed by the distribution of particle sizes and orientations.  $S_{\text{app}}(q)$  behaves as an apparent interparticle structure factor. In dilute systems, since  $S(q) = 1$ ,  $S_{\text{app}}(q) = 1$ .

It is known that self-assembly of small molecules and macromolecules in soft materials often forms fibrillar aggregates with various cross-sectional shapes. In the following sections, form factors of fibrillar aggregates with various cross-sectional shapes are briefly summarized.

#### Form Factor of Cylindrical Particles

Form factor  $P(q)$  of randomly oriented cylinders (rods) with radius  $R$  and length  $2H$ ,

$$P(q) = 4 \int_0^{\pi/2} \left[ \frac{\sin^2(qH \cos \beta)}{(qH \cos \beta)^2} \right] \left[ \frac{J_1^2(qR \sin \beta)}{(qR \sin \beta)^2} \right] \sin \beta d\beta, \quad (13.18)$$

where  $\beta$  is the angle between the scattering vector  $q$  and the axis of the cylinder, and  $J_1$  is the Bessel function of the first order. When the length of the fibrillar aggregates  $L$  is sufficiently long in comparison with the cross-sectional size,  $P(q)$  can be approximated by [2, 3]

$$P(q) = \frac{L\pi}{q} I_c(q). \quad (13.19)$$

There is a relation of  $L = 2H$ . Here  $I_c(q)$  represents the scattering intensity from cross section of cylindrical rod particles. In a  $q$  range much smaller than reciprocal of cross-sectional size but much larger than that of cylindrical rod length, i.e., for  $2\pi/L \ll q \ll 2\pi/R_c$ ,  $I_c(q)$  can be approximated by the Guinier type of representation,

$$I_c(q) = A^2 \exp\left(-\frac{R_c^2 q^2}{2}\right), \quad (13.20)$$

where  $R_c$  and  $A$  are the radius of the gyration and the area of the cross section of rod particles, respectively. Equation (13.20) is valid for cross section of arbitrary geometric shape. We can estimate  $R_c$  from slope in plot of  $\ln(Iq)$  vs.  $q^2$  [73, 74]. For circular cross section with monodisperse radius  $R$ , there is the following relation between  $R$  and  $R_c$ :

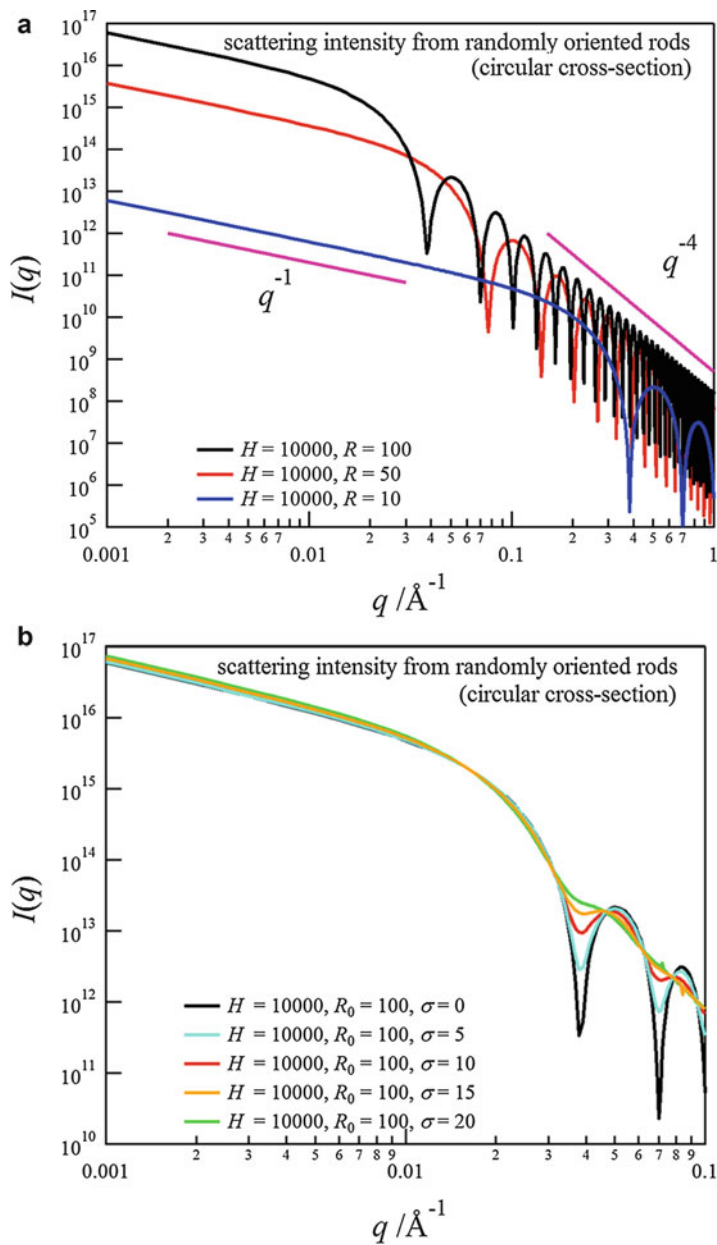
$$R_c = \frac{1}{\sqrt{2}}R. \quad (13.21a)$$

For particles with disk shape

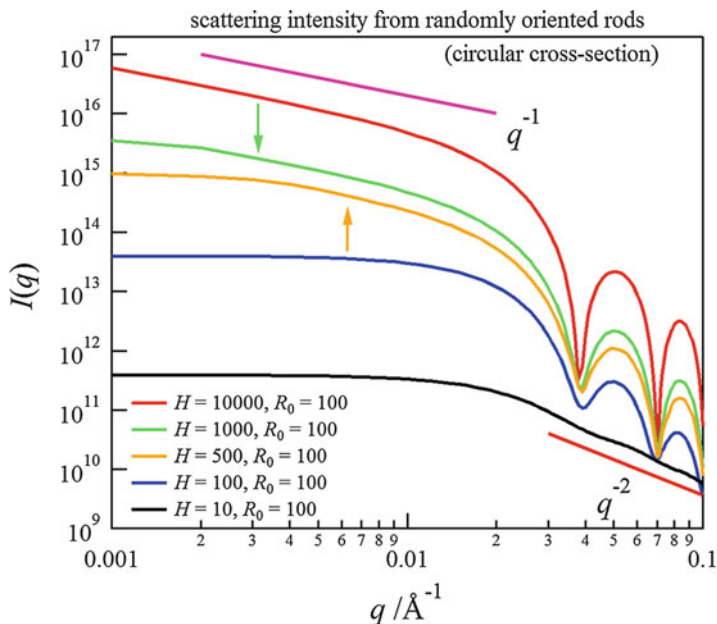
$$R_c = \frac{1}{\sqrt{3}}H = \frac{1}{\sqrt{12}}L, \quad (13.21b)$$

Figure 13.4a shows scattering functions ( $V_p^2 P(q)$ ) calculated without considering cross-sectional size distribution at various  $R$ 's. The position of the oscillation in the scattering functions shifts toward small  $q$  with increasing cross-sectional size. The scattering function in the small  $q$  range shows a behavior of  $q^{-1}$ , indicating the scattering from cylindrical rod particles. Equation (13.13) is applicable to cylindrical particles as well as spherical particles. Figure 13.4b depicts the scattering function with the Gaussian size distribution of  $R$ , where we put  $\Delta\rho^2 = 1$ ,  $n_p = 1$  in Eqs. (13.13) and (13.15). The oscillation becomes ambiguous with increase of the distribution of the cross-sectional size, i.e., with increase of  $\sigma$ . Thus, we can estimate the cross-sectional size of rod particles and the size distribution from a peak position and the broadness of a scattering profile [75].

Figure 13.5 presents scattering functions of cylindrical particles at various rod lengths. In the case of long cylindrical rods ( $H \gg R$ ), the scattering functions in the small  $q$  range have the behavior of  $I \propto q^{-1}$  as shown above. In a  $q$  range much smaller than  $2\pi/L$ , the scattering intensity becomes almost flat in the log-log plot.



**Fig. 13.4** Calculated scattering functions of monodisperse cylindrical particles at various  $R$ 's (a) and those of cylindrical particles with the Gaussian size distribution at various  $\sigma$ 's (b)



**Fig. 13.5** Calculated scattering functions of randomly oriented cylindrical particles with circular cross section at various lengths. The arrows in the figure represent the position of  $2\pi/L$

If  $R$  is much larger than  $H$ , i.e., cylindrical particles are regarded as disk particles rather than rod particles, the scattering function shows a behavior of  $q^{-2}$ .

Here let us show scattering curves of fibrillar aggregates formed by self-assembly of a low molecular weight organogelator in an organic solvent. Figure 13.6 shows combined SANS and focusing SANS profiles of 12-HSA/deuterated toluene gel over a wide temperature range from a gel state into a sol state [48].

The SANS data can be well described with the cylindrical form factor with the lognormal distribution (Eqs. (13.18) and (13.14)) over a broad  $q$  range. The fitted analysis leads to  $R_0 = 80 \text{ Å}$  and  $\sigma = 1.5$ , which hardly change by temperature and concentration variations. The SANS result indicates that these gels form fibrillar aggregates with almost the same thickness at various temperatures and concentrations.

### Form Factor of Rod Particles with Rectangular Cross Section

When the cross section has a rectangular shape of the lengths of the sides  $a$  and  $b$ ,  $I_c(q)$  is presented by [76]

$$I_c = \frac{2}{\pi} \int_0^{\pi/2} \left[ \frac{\sin(qa \sin \beta/2)}{qa \sin \beta/2} \right]^2 \left[ \frac{\sin(qb \cos \beta/2)}{qb \cos \beta/2} \right]^2 d\beta. \quad (13.22)$$

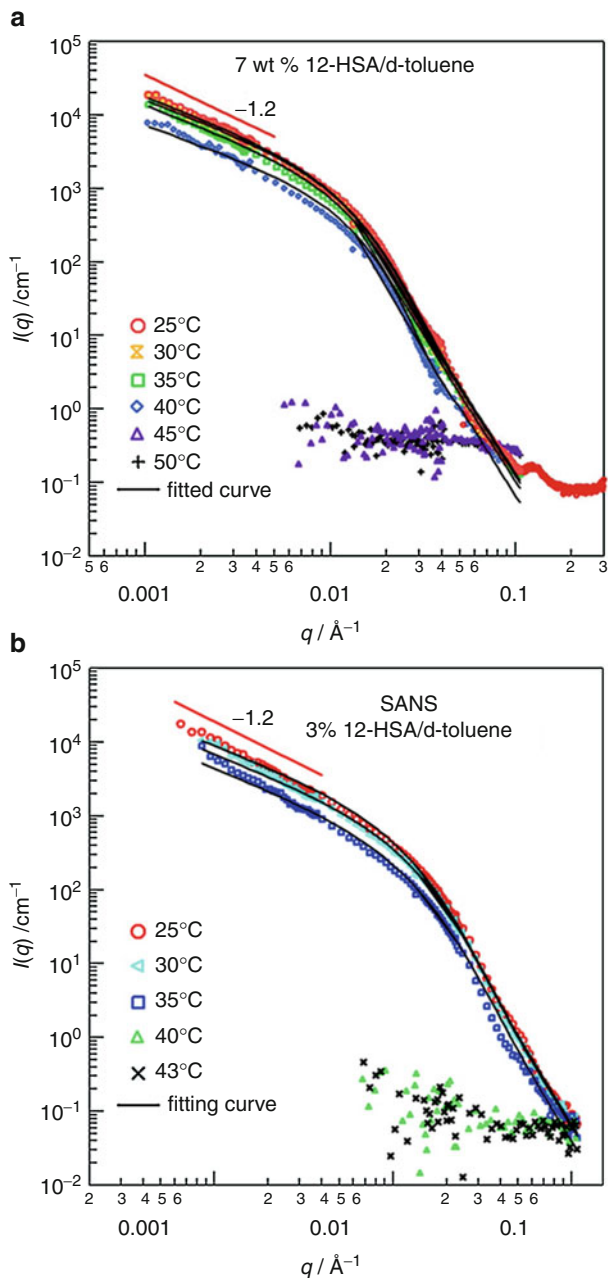


**Fig. 13.6** SANS profiles at various temperatures for (a) 7 wt % 12-HSA gel and (b) 3 wt % 12-HSA gel. The solid lines represent the fitted curves (Reproduced with permission from *J Phys Chem B* [48]. Copyright (2012) American Chemical Society)

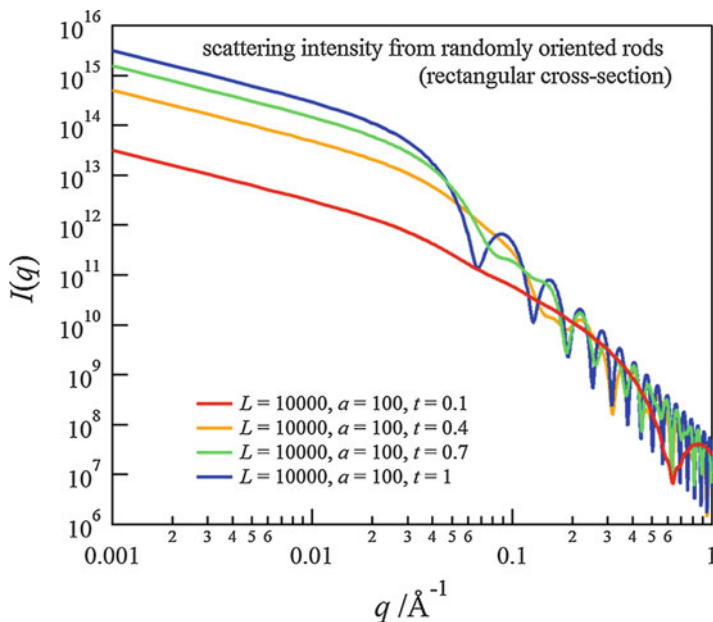


**Fig. 13.7** Scattering profiles calculated with scattering function from rectangular cross section with ratio of  $t = b/a$

Figure 13.7 depicts theoretical curves calculated with the scattering function from rectangular cross section at various ratios of  $t = b/a$ . The periodicity of the oscillation is modulated by variation of  $t$ .

### Form Factor of Long Helices

Cross section of fibrillar aggregates has a variety of shapes such as hollow tube, helical ribbon, and double tube superhelix other than circular and rectangular cross sections [77–80]. The scattering function for infinitely long helices was derived by Pringle and Schmidt, which covers single, double, and hollow helices [81]. This model has been applied to various systems forming helical aggregates [79, 82, 83]. The scattering function can be described in the following form:

$$I(q) = \frac{\pi}{qL} \sum_{n=0}^{\infty} \varepsilon_n \cos^2(n\varphi/2) \frac{\text{Sin}^2(n\omega/2)}{(n\omega/2)^2} [g_n(qR, a)]^2 \tag{13.23a}$$

where

$$g_n(qR, a) = 2R^{-2}(1 - a^2)^{-1} \int_{aR}^R r J_n\left(qr\sqrt{1 - q_n^2}\right) dr \tag{13.23b}$$

$$q_n = \frac{nb}{qR} \text{ for } qR \geq nb \quad (13.23c)$$

$$q_n = 1 \text{ for } qR \leq nb \quad (13.23d)$$

$$b = \frac{2\pi R}{P} \quad (13.23e)$$

$$\varepsilon_0 = 1 \text{ and } \varepsilon_n = 2 \text{ for } n \geq 1. \quad (13.23f)$$

$J_n(x)$  is the Bessel function of the first kind and order of  $n$ .  $L$  and  $P$  are the total length of the helix with its outer radius  $R$  and its inner radius  $aR$  and the helix period, respectively. The parameters  $\varphi$  and  $\omega$  are the angle between the two sectors of a double helix and the angular part of the sector of a material, respectively. Although the summation in Eq. (13.23a) is described as infinite series, as a matter of fact, the terms for  $n \geq qR/b$ , i.e.,  $n \geq Pq/2\pi$ , are zero.

The model can be extended to a helical tape consisted of  $N$  layers as shown by Teixeira et al. [82]. For a single helical tape with  $N$  shells (in this case  $\varphi = 0$ ), the form factor of the helical tape can be expressed by

$$I(q) = \frac{\pi}{qLC_{n-shell}^2} \sum_{n=0}^{\infty} \varepsilon_n \frac{\text{Sin}^2(n\omega/2)}{(n\omega/2)^2} [G_{shell, n}(R_m, \rho_m, P, q)]^2 \quad (13.24)$$

with

$$G_{shell, n}(R_m, \rho_m, P, q) = \sum_{m=1}^N (\rho_m - \rho_{m-1}) \times 2 \int_0^{R_m} r J_n(qr \sqrt{1 - q_n^2}) dr \quad (13.25)$$

and

$$C_{n-shell} = \sum_{m=1}^N (\rho_m - \rho_{m-1}) R_m^2, \quad (13.26)$$

where  $R_m$  represents the radius of shell  $m$  with electron density  $\rho_m$ .

Teixeira et al. tried to fit theoretical scattering functions from helical model and from polydisperse cylindrical model to the scattering data from nanotube of hexa-*peri*-hexabenzocoronene (HBC)-based molecules in THF. They showed that the helical model with hexagonal structure factor is superior to the polydisperse cylindrical model in the fit of their SAXS data. The scattering curves from the helical model represent the width of the oscillator and the depth of the minima of the data very well as shown in Fig. 13.8.

Other than these models, recently, form factor of helical ribbons was derived by Hamley [84].



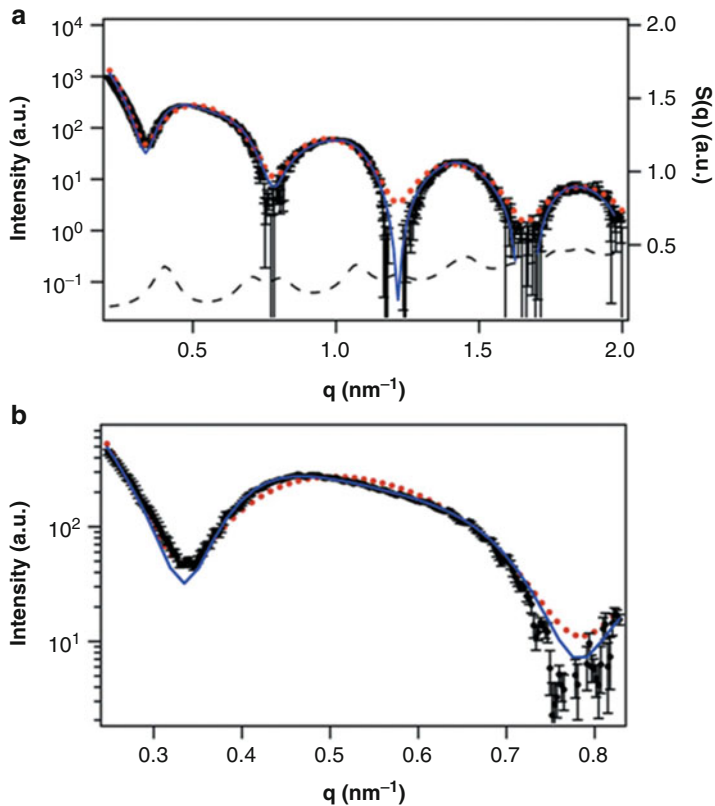


**Fig. 13.8** Scattering curve of hexa-*peri*-hexabenzocoronene (HBC)/THF. Experimental curve (black), helix form factor (red), hexagonal structure factor (right axis; dashed line) (Reproduced with permission from *J Appl Crystallogr* [82]. Copyright (2010) International Union of Crystallography)

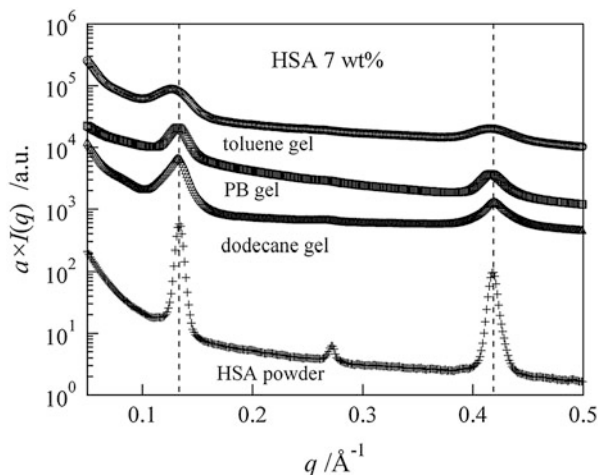
### 5.2.3 Structures at High $q$

Scattering intensity at high  $q$  follows the Porod law, which describes the scattering behavior from the interface of the particles [3, 4], and it comes from thermal concentration fluctuations (TCFs) inside the phase in the case of phase-separated systems:

$$I(q) = \frac{(\Delta\rho)^2 2\pi S}{q^4} + I_{\text{TCF}}, \quad (13.27)$$

where  $S$  is the total surface area of the particles. The scattering behavior from TCFs can be described by the Ornstein–Zernike representation,

**Fig. 13.9** Synchrotron SAXS profiles of 12-HSA powder and 7 wt % 12-HSA gel in PB oligomer, toluene, and dodecane. *Dashed lines* at  $q = 0.13 \text{ \AA}^{-1}$  and  $q = 0.41 \text{ \AA}^{-1}$  denote (001) and (003) Bragg reflections, respectively (Reproduced with permission from *Prog Colloid Polym Sci* [47]. Copyright (2009) Springer-Verlag, Berlin Heidelberg)



$$I_{\text{TCF}} = \frac{I_0}{1 + \xi^2 q^2} \quad (13.28)$$

where  $I_0$  is a prefactor and  $\xi$  is the correlation length of TCFs. In the case of polymer blends or polymer solutions, the scattering intensity from TCFs obeys the scattering function calculated on the basis of the random phase approximation [85, 86].

If the aggregates exhibit a crystalline nature, e.g., self-assembled aggregates of some LMOGs form crystalline fibers [46, 47, 87, 88], then the Bragg peaks are observed, e.g., long spacing of fatty acids with long alkyl chains is usually in the range of 3–5 nm measurable in the SAXS experiments. Figure 13.9 depicts comparison of SAXS profiles between 12-HSA gels in various solvents and the powder. As shown in the figure, the profiles of gels for various solvents have the Bragg peaks corresponding to (001) and (003) reflections at the same positions as the powder sample (without any solvents), indicating that molecular arrangement of the LMOG in the gel is similar to that of the crystalline powder. Wide-angle X-ray scattering (WAXS) profiles for the gel also have the Bragg peaks at the same positions as the crystalline powder [88]. Other than the  $q$ -dependent coherent scattering part as shown above, the SANS intensity contains a  $q$ -independent incoherent scattering part. Usually it is treated as background scattering in the SANS measurements, although the incoherent scattering contains important dynamical information regarding molecular vibrations and the rotations in neutron spectroscopy such as inelastic and quasi-elastic neutron scattering measurements [4, 89].

#### 5.2.4 Unified Approach of Multilevel Structures

The Beaucage unified model [63–66] is used to analyze multilevel structures investigated by combined various small-angle scattering measurements [43, 51, 52, 69,

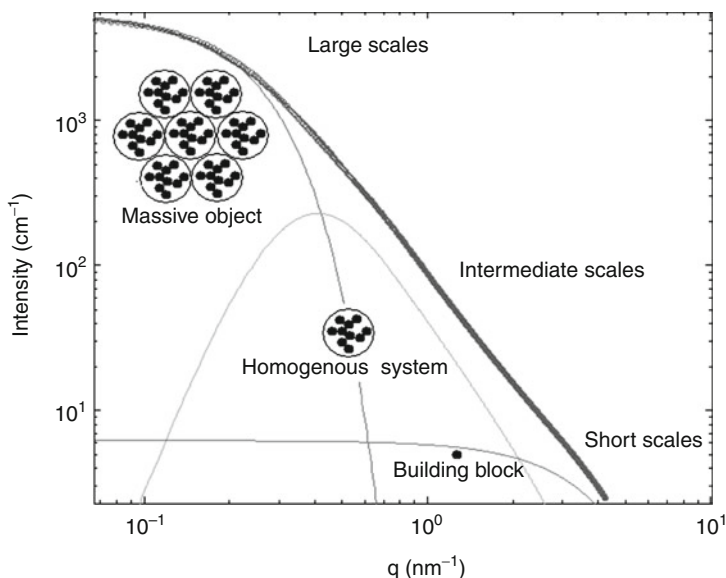


**Fig. 13.10** A SAXS profile of an inorganic titania-based gel fitted with the Beaucage model (Reproduced with permission from *J Phys Chem B* [91]. Copyright (2010) American Chemical Society)

90, 91]. The model describes a smooth transition between the Guinier regime and a power-law regime such as the Porod regime. It can be extended to represent an arbitrary number of structures at different size scales,

$$I(q) = \sum_{i=1}^n \left( G_i \exp\left(\frac{-q^2 R_{g,i}^2}{3}\right) + B_i \exp\left(\frac{-q^2 R_{g,i+1}^2}{3}\right) \times \left\{ \frac{\left[ \operatorname{erf}\left(\frac{q R_{g,i}}{\delta^{1/2}}\right) \right]^3}{q} \right\}^{P_i} \right), \quad (13.29)$$

where  $G_i$ ,  $B_i$ ,  $R_{g,i}$ , and  $P_i$  represent the Guinier prefactor, a prefactor specific to the power-law scattering, the radius of gyration of the  $i$ -th level structure, and the exponent of the power-law scattering, respectively. In Eq. (13.29),  $i = 1$  refers to the largest-size structural level. If the power-law scattering of the  $i$ -th level structure obeys the Porod law, then  $P_i = 4$  and  $B_i = 2\pi(\Delta\rho)^2 S$ . The Beaucage model was recently compared with other models in depth by Hammouda [70, 71].

Pattier et al. investigated the structure of inorganic titania-based gels by SAXS and analyzed the SAXS data with the Beaucage model [91]. Figure 13.10 shows the SAXS data of an inorganic titania-based gel and the curve fitted with the Beaucage model. The Beaucage model well describes the multilevel structure of the gel.

### 5.3 Contrast-Matching and Contrast Variation Methods in SANS and SAXS

Contrast-matching [92–97] and contrast variation [16, 98–101] methods have so far been widely used to study complex structures of multicomponent systems. These methods are usually carried out by changing scattering length density of solvents. In the case of SAXS, the contrast variation experiments have been performed by changing the electron density of the solvent using substances inactive for latex particles, proteins, or macromolecules [3, 11, 102–104]. Substances such as sucrose and glycerol are often used as additives for the contrast variation. However, application of this method can be implemented only in a limited range, since addition of a substance for contrast variation may affect structures of the scattering objects. Otherwise anomalous or resonant contrast variation method is effective [16, 105]. Generally, the scattering length of a substance is an energy-dependent complex quantity and can be changed through variation of energies of incident X-ray near absorption edge of elements. Application of anomalous SAXS contrast variation method has been performed for various polymeric systems [64, 106–111]. The details of the anomalous SAXS method will be described in details in Sect. 5.3.4.

In the SANS experiments, contrast variation or contrast-matching methods are very effective to probe internal structures in multicomponent complex systems, since neutron scattering length of deuterium is largely different from that of hydrogen as mentioned in the Introduction. Therefore, hydrogen/deuterium replacement can easily change SANS contrast almost without modification of their chemical properties. This SANS contrast variation method has been widely utilized in various soft materials such as colloids, polymers, composites of polymer–inorganic substances, and biological systems. In the following sections, we shall describe details of SANS and SAXS contrast variation methods and the recent application.

#### 5.3.1 Scattering Equation of Multicomponent Systems

The scattering intensity from the multicomponent systems with different  $(p + 1)$  species ( $0 \leq i \leq p$ ) can be described in the following form [4]:

$$I(q) = \sum_{i=0}^p \rho_i^2 S_{ii}(q) + 2 \sum_{i<j}^p \rho_i \rho_j S_{ij}(q) \quad (13.30)$$

$\rho_i$  is the scattering length density for  $i$ -th component, and  $S_{ij}$  is the partial structure factor, which is defined by

$$S_{ij}(q) = \iint n_i(r) n_j(r') \exp[-iq \cdot (r' - r)] dr dr' \quad (13.31)$$

where  $n_i(r)$  is the local density of component  $i$  at a position  $r$ . On the incompressible assumption, Eq. (13.30) is reduced to the following form:

$$I(q) = \sum_{i=1}^p (\rho_i - \rho_0)^2 S_{ii}(q) + 2 \sum_{i<j} (\rho_i - \rho_0)(\rho_j - \rho_0) S_{ij}(q). \quad (13.32)$$

Thus, the scattering intensity of multicomponent systems is composed of both self-terms and cross-terms of the partial structure factors. For the ternary system, the scattering intensity can be expressed by

$$I(q) = (\rho_1 - \rho_0)^2 S_{11}(q) + (\rho_2 - \rho_0)^2 S_{22}(q) + 2(\rho_1 - \rho_0)(\rho_2 - \rho_0)S_{12}(q) \quad (13.33)$$

### 5.3.2 SANS Contrast-Matching and Contrast Variation Methods

In the small-angle scattering, the scattering length density is calculated from the chemical composition of the particles or the molecules.

$$\rho = \frac{\sum b_i}{v}, \quad (13.34)$$

where  $v$  and  $b_i$  are the volume considered in the chemical composition and the scattering length of the component  $i$ , respectively. Using the values of the scattering length shown in Table 13.1, it turns out that the neutron scattering length density of  $\text{H}_2\text{O}$  ( $\rho_{\text{H}_2\text{O}} = -5.62 \times 10^9 \text{ cm}^{-2}$ ) is largely different from that of  $\text{D}_2\text{O}$  ( $\rho_{\text{D}_2\text{O}} = 6.40 \times 10^{10} \text{ cm}^{-2}$ ), while the X-ray scattering length of heavy water and light water is  $9.44 \times 10^{10} \text{ cm}^{-2}$ . Thus, in SANS measurements we can easily change the scattering contrast of aqueous systems by adjusting mixing ratio between  $\text{H}_2\text{O}$  and  $\text{D}_2\text{O}$ .

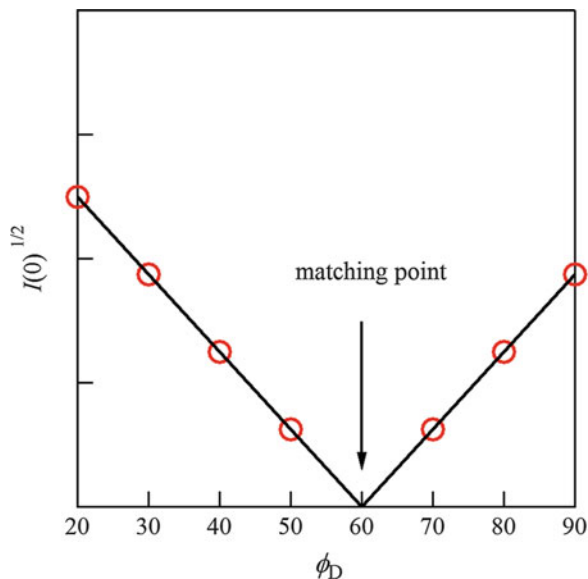
First of all, let us consider a three-component system composed of an inorganic nanoparticle, a polymer, and a solvent (water). Here if components 0, 1, and 2 denote solvent, inorganic nanoparticle, and polymer, respectively, and the scattering contrast between the inorganic nanoparticle and the solvent is matched, i.e.,  $\rho_i = \rho_s$ , then Eq. (13.33) leads to

$$I(q) = (\rho_p - \rho_s)^2 S_{pp}(q). \quad (13.35)$$

Here subscripts  $i$ ,  $p$ , and  $s$  denote inorganic nanoparticle, polymer, and solvent species, respectively.

In order to determine the scattering length density of the inorganic nanoparticles, the scattering intensity from the nanoparticles dispersed in  $\text{H}_2\text{O}/\text{D}_2\text{O}$  is measured. Since the scattering intensity  $I(0)$  at  $q = 0$  is proportional to the square of the scattering contrast as shown in Eq. (13.10), there is a linear relationship between  $\sqrt{I(0)}$  and  $\Delta\rho$ . Therefore, the matching point can be obtained from a plot of  $\sqrt{I(0)}$  vs.  $\phi_{\text{D}}$  as shown in Fig. 13.11 [10]. Or it can be obtained from a fit to the scattering intensity with a quadratic function [95, 112]. In the case of  $\text{SiO}_2$ , since  $\rho_{\text{SiO}_2} \cong 3.59 \times 10^{10} \text{ cm}^{-2}$ , the scattering length density of the silica particles is matched by  $\sim 40/60$  mixture of  $\text{H}_2\text{O}/\text{D}_2\text{O}$  [96]. If H/D exchange occurs on the inorganic nanoparticles, the scattering length density varies with the fraction of  $\text{D}_2\text{O}$  [113].

**Fig. 13.11** A plot of square of the scattering intensity vs. fraction of deuterated solvent to obtain contrast-matching point



Contrast-matching SANS presents information on the chain conformation in a polymer nanocomposite [95]. However, if the inorganic nanoparticles are not homogeneous/inorganic, it is difficult to perfectly match the scattering contrast [95]. In a similar manner, contrast matching of a polymer and a solvent is also possible [114].

In the case of contrast variation method, scattering experiments with different scattering contrasts, e.g., changing ratio of  $\text{H}_2\text{O}/\text{D}_2\text{O}$  in aqueous systems are carried out.

Recently, Endo et al. developed SANS contrast variation method to evaluate partial structure factors in multicomponent systems such as microemulsion systems or block copolymer systems including inorganic materials [99, 100, 115]. Now, assuming that scattering measurements with  $n$  different contrasts are conducted, scattering intensity for each measurement can be expressed as follows:

$$\mathbf{I} = \mathbf{M} \cdot \mathbf{S} \quad (13.36)$$

where  $\mathbf{I}$  represents a vector of the scattering intensities at  $n$  different scattering contrasts, i.e.,

$$\mathbf{I} = \begin{pmatrix} I_1(q) \\ \vdots \\ I_n(q) \end{pmatrix} \quad (13.37)$$

and  $\mathbf{M}$  is a matrix related to scattering contrasts composed of the following form for ternary systems,

$$\mathbf{M} = \begin{pmatrix} {}^1\Delta\rho_1^2 & 2^1\Delta\rho_1^1\Delta\rho_2 & {}^1\Delta\rho_2^2 \\ \vdots & \vdots & \vdots \\ {}^n\Delta\rho_1^2 & 2^n\Delta\rho_1^n\Delta\rho_2 & {}^n\Delta\rho_2^2 \end{pmatrix} \quad (13.38)$$

with

$${}^j\Delta\rho_1 = \rho_1 - {}^j\rho_0 \quad (13.39)$$

and

$${}^j\Delta\rho_2 = \rho_2 - {}^j\rho_0 \quad (13.40)$$

where  ${}^j\rho_0$  is a scattering length density of the solvent in the  $j$ -th experiments ( $j = 1, \dots, n$ ).

$\mathbf{S}$  denotes a vector of partial structure factors

$$\mathbf{S} = \begin{pmatrix} S_{11}(q) \\ S_{12}(q) \\ S_{22}(q) \end{pmatrix} \quad (13.41)$$

Thus, the partial structure factors can be obtained using orthogonal matrix  $\mathbf{M}^T$  from Eq. (13.36):

$$\mathbf{S} = \mathbf{M}^T \cdot \mathbf{I} \quad (13.42)$$

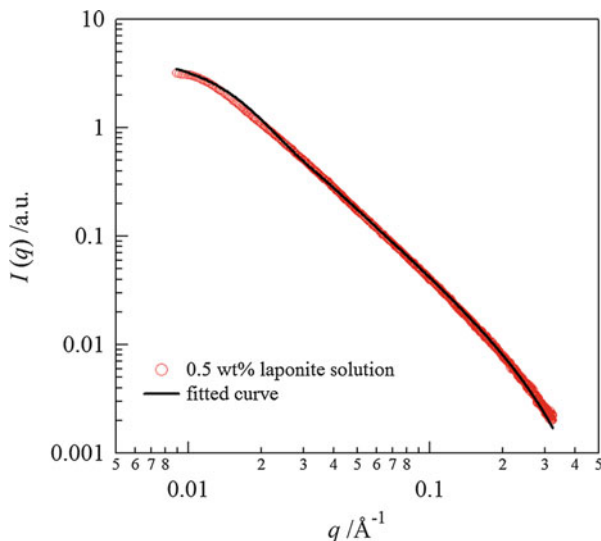
This sophisticated method has been applied to various soft materials such as polymer–clay nanocomposite hydrogels [101, 116, 117], rubber-filler systems [52, 53], polymer–inorganic particles, and fuel cells [118].

### 5.3.3 Application in Contrast Variation SANS Method

Recently, a variety of polymer nanocomposite systems have attracted many researchers from a viewpoint of potential application of materials in various fields. Accordingly, numerous studies have been made on polymer–inorganic nanocomposites [18, 52, 119], polymer–clay nanocomposite hydrogels [97, 119, 120], rubber-filler systems [18, 52, 121], and polymer–graphene composites [121–123]. Composite of polymer and inorganic substances causes enhancement of material properties such as thermal, mechanical, self-healing, and electrical properties. Recent SAXS, SANS, USAXS, and USANS studies reveal that these scattering methods are very useful to investigate structures of polymer nanocomposite materials.

Here let us show a structural analysis of polymer–clay nanocomposite hydrogels using the above contrast variation method. Haraguchi et al. developed polymer–clay nanocomposite hydrogels with excellent properties such as high extensibility, mechanical toughness, and self-healing by using in situ free radical polymerization

**Fig. 13.12** The SAXS profile of a 0.5 wt% Laponite aqueous solution. The *solid curve* represents the curve fitted with Eq. (13.18), considering the inhomogeneity of the radius of clay particles with the Gaussian distribution (Eq. 13.15) (Reproduced with permission from *Colloid Polym Sci* [130]. Copyright (2013) Springer, Berlin/Heidelberg)



of *N*-alkylacrylamide in the presence of inorganic clay [124–128]. More recently, polymer–clay nanocomposite hydrogels with excellent mechanical properties were fabricated by simple mixing of clay with a cationic dendrimer [129] and a commercially available anionic polymer [130]. Since these materials are multicomponent, contrast variation method is useful. Synthetic hectorite (Laponite from Rockwood Ltd.) used as inorganic clay is a colloidal layered silicate made of the chemical composition of  $\text{Na}_{0.66}[\text{Mg}_{5.34}\text{Li}_{0.66}\text{Si}_8\text{O}_{20}(\text{OH})_4]$ . The clay particles have a disk-shaped structure with a radius of 130–150 Å and thickness of 10 Å [59, 60, 130]. Figure 13.12 shows a SAXS profile for a 0.5 wt % Laponite aqueous solution. The profile can be well described by the form factor of cylindrical particles (Eq. 13.18) with radius of 130 Å and thickness of 10 Å with the Gaussian distribution (Eq. 13.15) in the radius ( $\sigma = 30$  Å) [130].

The scattering contrast of the nanocomposite hydrogel in SANS can be easily changed by variation of mixing ratios between light water and heavy water. Endo, Shibayama, and Haraguchi et al. investigated structures of clay (Laponite)–poly(*N*-isopropylacrylamide) (PNIPAM) nanocomposite hydrogels with the sophisticated contrast variation SANS as shown in the previous section [101, 131]. They obtained the partial structure factors  $S_{cc}(q)$ ,  $S_{cp}(q)$ , and  $S_{pp}(q)$  from the scattering functions of samples prepared at seven different  $\text{H}_2\text{O}/\text{D}_2\text{O}$  ratios (Fig. 13.13a). Here the subscript *c* represents clay.

The scattering curves reconstructed from the partial structure factors obtained thus are in good agreement with the original experimental SANS curves (Fig. 13.13b).

Taking into consideration a layer of polymer chains adsorbed on clay particles as shown in Fig. 13.14, they analyzed the partial structure factors obtained from the contrast variation SANS.



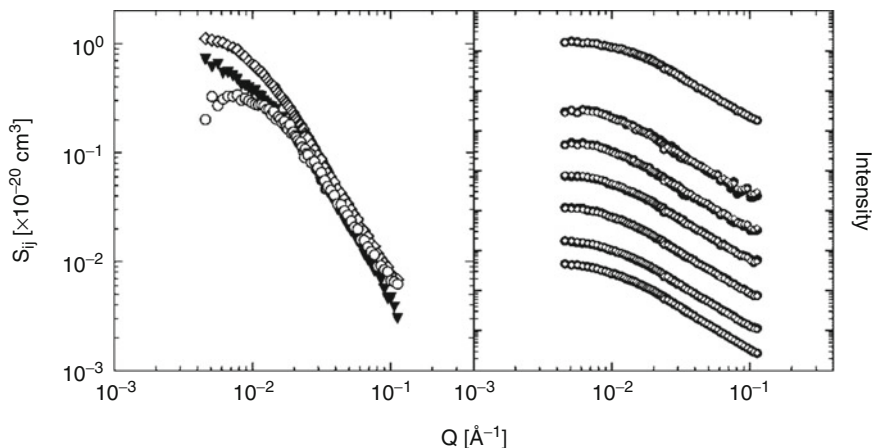
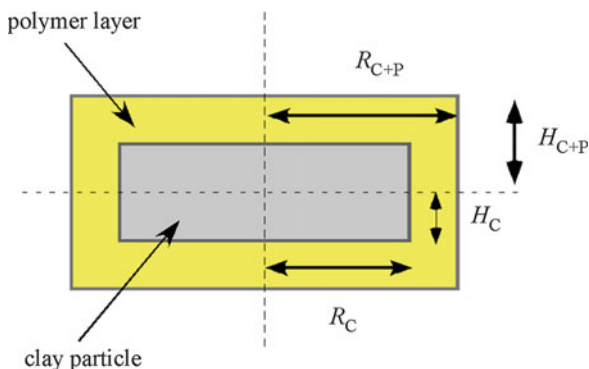


**Fig. 13.13** (a) The partial structure factor obtained from Eq. (13.42); circle ( $S_{cc}$ ), filled inverse triangle ( $S_{cp}$ ), lozenge ( $S_{pp}$ ). (b) Comparison between reconstructed scattering curves (lozenge) and experimental scattering curves (solid circle) (Reproduced with permission from *Macromolecules* [131]. Copyright (2008) American Chemical Society)

**Fig. 13.14** A schematic illustration of a model of polymer layer adsorbed on clay particles



As the clay is cylindrical disk-shaped particles, the scattering amplitude of clay particles  $F_c$  is presented in the following form:

$$F_c(q) = 2 \frac{\sin(qH \cos \beta)}{qH \cos \beta} \frac{J_1(qR \sin \beta)}{qR \sin \beta} \quad (13.43)$$

$\beta$  and  $J_1$  are the same in Eq. (13.18).

The partial structure factor  $S_{cc}(q)$  is written as follows:

$$S_{cc}(q) = n_c V_c^2 P_c(q) S_{c,app}(q) \quad (13.44)$$

$P_c(q)$  and  $S_{c,app}(q)$  are the form factor of clay particles and the apparent structure factor, which are described by Eqs. (13.18) and (13.17), respectively. The partial

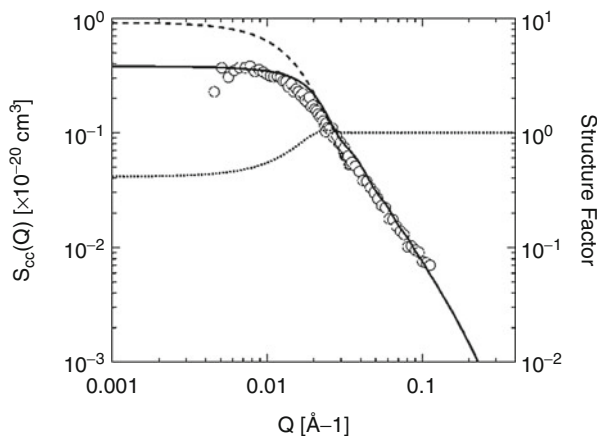


**Fig. 13.15** Comparison between the partial structure factor  $S_{cc}(q)$  and the fitted curve. The *broken* and the *dotted* curves show the form factor and the apparent structure factor, respectively (Reproduced with permission from *Macromolecules* [131]. Copyright (2008) American Chemical Society)

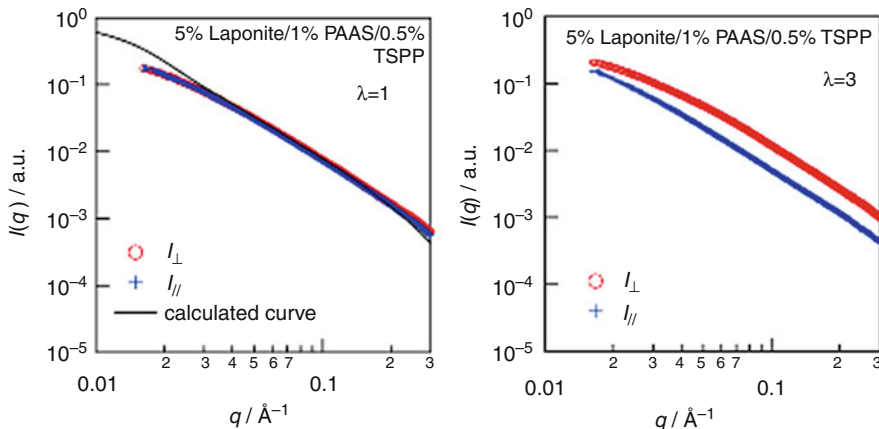
structure factor of polymer  $S_{pp}(q)$  is composed of two contributions from the polymer adsorption layer and from the polymer network, which can be usually represented by the Lorentz function such as Eq. (13.28).

Figure 13.15 shows the analytical result of  $S_{cc}(q)$  by Endo et al. The  $S_{cc}(q)$  corresponds with the form factor of clay particles (broken curve) in high  $q$  range, while it deviates downward in a small  $q$  range due to effect of interparticle interference, i.e.,  $S_{app}(q)$ .

The partial structure factor  $S_{cc}(q)$  is similar to the overall SAXS profile of a clay–anionic polymer nanocomposite hydrogel for an unstretched sample as shown in Fig. 13.16 in spite of use of different polymer species, where the solid curve represents the form factor of cylindrical disk particles. The SAXS intensity in the small  $q$  range is also suppressed due to the interparticle interference in comparison with the form factor. Since clay particles are constituted of heavy atoms relative to polymers and water, the SAXS intensity of the polymer–clay nanocomposite hydrogel comes mainly from clay particles [130].

On the other hand, the cross-term  $S_{cp}(q)$  reflects the structure of the adsorption layer. If there is no correlation between polymer and clay particles, i.e., no adsorption layer,  $S_{cp}(q)$  becomes negative [99]. In fact,  $S_{cp}(q)$  is positive as shown in Fig. 13.13. Thus, Endo et al. showed that the polymer chains are strongly adsorbed on the surfaces of clay particles from the analysis of the partial structure factor  $S_{cp}(q)$  [131].

The sophisticated contrast variation SANS method is effective for other multicomponent systems. Takenaka et al. carried out structural analysis by using the contrast variation SANS method for swollen rubber–silica and rubber–carbon black systems, considering a polymer layer adsorbed on the particles [52, 53]. They



**Fig. 13.16** SAXS profiles of a clay–anionic polymer nanocomposite hydrogel; *left* before stretching, *right* after stretching. The *solid line* represents the form factor of the randomly oriented disklike particles ( $R = 13$  nm,  $\sigma = 3$  nm, and  $2H = 1.0$  nm) (Reproduced with permission from *Colloid Polym Sci* [130]. Copyright (2013) Springer, Berlin/Heidelberg)

adopted the Beaucage model for analysis of partial structure factors obtained with the contrast variation SANS and estimated structural parameters regarding interfacial properties in the rubber–filler systems.

### 5.3.4 Contrast Variation in SAXS: Anomalous SAXS

When SAXS measurements were conducted near absorption edge of elements, the scattering length  $f(E)$  becomes a complex quantity as shown in Fig. 13.17 [132, 133]:

$$f(E) = f_0 + f'(E) + if''(E), \tag{13.45}$$

where  $f_0$  is the nonresonant term which is proportional to the atomic number of the element and the resonant terms  $f'(E)$  and  $f''(E)$  are the real and imaginary components of the energy-dependent anomalous dispersion.

When anomalous SAXS measurements are performed, the scattering amplitude  $F(q, E)$  is composed of two parts as follows [134]:

$$F(q, E) = \int \Delta\rho_0(\mathbf{r})\exp(-i\mathbf{q}\mathbf{r})d\mathbf{r} + \int \Delta\rho_R(\mathbf{r}, E)\exp(-i\mathbf{q}\mathbf{r})d\mathbf{r} \tag{13.46}$$

where  $\Delta\rho_0$  and  $\Delta\rho_R$  are the electron density difference of the nonresonant and the resonant scattering atoms.

In the past, anomalous SAXS has been mainly applied to hard materials such as ceramics, metal catalyst, and metal alloys, which are composed of elements with a

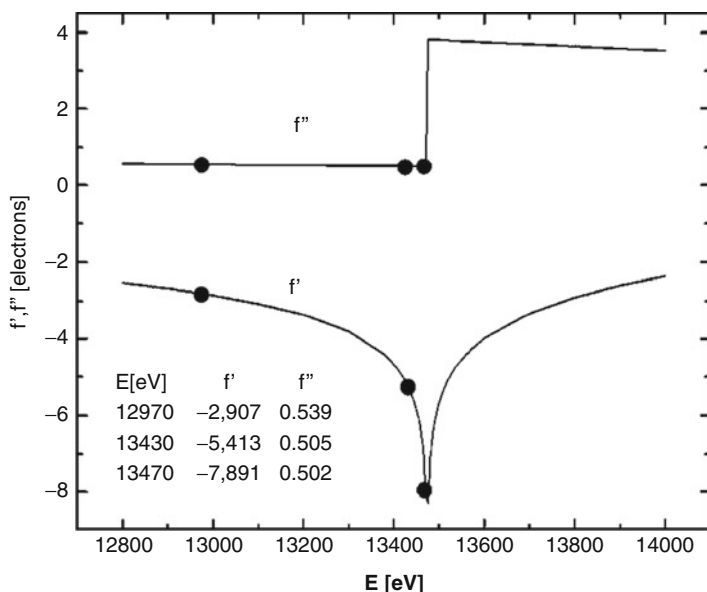


**Fig. 13.17** Anomalous scattering factors of bromine (Reproduced with permission from *J Phys Chem B* [132]. Copyright (2006) American Chemical Society)

high atomic number [135–139]. This is because the absorption edge of the elements with high atomic number could be easily reached in the energy range of synchrotron X-rays. In the case of polymeric systems, the distribution and the number of counterion around a polyelectrolyte and DNA can be probed by anomalous SAXS [107, 109, 140]. Otherwise, absorption edge of K shell of bromine (Br) is often utilized [106, 132, 141, 142]. As mentioned above, the scattering amplitude  $F(q, E)$  consists of two contributions of the nonresonant and resonant terms ( $F_0(q)$  and  $F_R(q, E)$ ):

$$F(q, E) = F_0(q) + F_R(q, E). \quad (13.47)$$

When the measurement is performed near the absorption edge of K shell of Br,  $F_R(q, E)$  can be written as follows:

$$F_R(q, E) = [f'_{Br}(E) + if''_{Br}(E)]V(q). \quad (13.48)$$

$V(q)$  corresponds to the Fourier transform of the distribution function of Br, i.e.,  $V^2(q)$  corresponds to the form factor derived from the spatial distribution of Br.

Using Eq. (13.10), the anomalous scattering intensity  $I(q, E)$  is presented by [106, 143]

$$I(q) = n_P V_P^2 \left[ F_0^2(q) + 2f'_{Br}(E) F_0(q) V(q) + \left\{ f''^2_{Br}(E) + f''^2_{Br}(E) \right\} V^2(q) \right] S(q) \quad (13.49)$$

since  $P(q, E) = F(q, E) F(q, E)^*$ . In dilute systems,  $S(q)$  approaches 1 as mentioned above. In practice  $V^2(q)$  can be obtained from difference between different scattering profiles measured at different energies [106]. The difference in the scattering intensities at two different energies ( $E_i$  and  $E_j$ ),  $\Delta I_{ij}$ , is represented as follows:

$$\Delta I_{ij}(q, E_i, E_j) = n_P V_P^2 \left[ 2 \{ f'_{Br}(E_i) - f'_{Br}(E_j) \} F_0(q) V(q) + \left\{ f''^2_{Br}(E_i) - f''^2_{Br}(E_j) + f''^2_{Br}(E_i) - f''^2_{Br}(E_j) \right\} V^2(q) \right], \quad (13.50)$$

assuming  $S(q) = 1$ . Thus, using the scattering intensity measured at three different energies of X-rays ( $E_1, E_2, E_3$ ),  $V^2(q)$  can be obtained in the following form:

$$V^2(q) = \frac{1}{K} \left[ \frac{\Delta I_{12}(q, E_1, E_2)}{f'_{Br}(E_1) - f'_{Br}(E_2)} - \frac{\Delta I_{13}(q, E_1, E_3)}{f'_{Br}(E_1) - f'_{Br}(E_3)} \right] \quad (13.51)$$

with

$$K = f'_{Br}(E_2) - f'_{Br}(E_3) + \frac{f''^2_{Br}(E_1) - f''^2_{Br}(E_2)}{f'_{Br}(E_1) - f'_{Br}(E_2)} - \frac{f''^2_{Br}(E_1) - f''^2_{Br}(E_3)}{f'_{Br}(E_1) - f'_{Br}(E_3)} \quad (13.52)$$

Akiba et al. performed anomalous SAXS measurements at three different energies of incident X-rays near the absorption edge of bromine (13.473 keV, 13.453 keV, 13.283 keV) in order to probe the internal structure of polymer micelles comprising poly(4-bromostyrene)-*block*-poly(ethylene glycol)-*block*-poly(4-bromostyrene) in an aqueous solution [106].  $V^2(q)$  obtained from the above analysis is shown in Fig. 13.18. The solid curve in Fig. 13.18 represents the scattering function calculated for a sphere with the radius of 10.2 nm, which is in good agreement with the data. Thus, the anomalous SAXS analysis revealed that the core composed of poly(4-bromostyrene) chains formed sphere with the radius of 10.2 nm.

## 5.4 Time-Resolved Scattering Measurements

Aggregated structures are developed via various processes such as liquid–liquid phase separation, crystallization, gelation, and micellization. Investigation of the kinetics is very important in order to understand the mechanism of their processes. Time-resolved scattering measurements have been performed for investigation of such kinetics. Especially, synchrotron SAXS technique is a very powerful tool to pursue a fast process, since high brilliance of synchrotron radiation makes it possible to obtain such precise data at a very short accumulation time [144, 145].

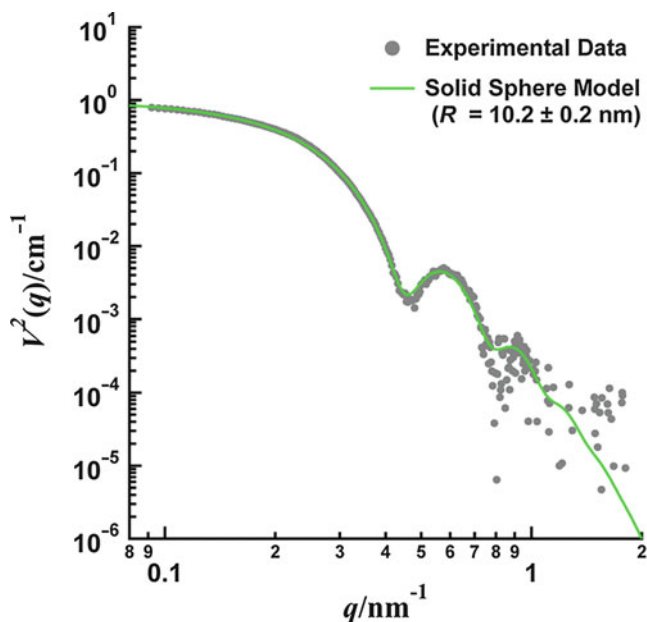


**Fig. 13.18** Resonant term  $V^2(q)$  of poly(4-bromostyrene)-*block*-poly(ethylene glycol)-*block*-poly(4-bromostyrene) micelles (Reproduced with permission from *Macromolecules* [106]. Copyright (2012) American Chemical Society)

Time-resolved SANS measurements also may be useful in some cases [146–151], although neutron sources are inherently weaker than synchrotron X-ray sources. Sometimes repeating experiments are performed in order to overcome a poor statistical accuracy, and the average scattering data are analyzed [149–151]. However, recent development of neutron sources makes it possible to follow the kinetics with a time resolution of subsecond [146, 152, 153]. Time-resolved synchrotron SAXS/SANS measurements are performed with specific cells such as temperature-jump or pressure-jump cells designed for synchrotron SAXS/SANS experiments [154, 155]. In synchrotron SAXS experiments, it is necessary to operate the cell by remote control outside a hutch.

Here we shall show a gelation process of a LMOG investigated by using time-resolved synchrotron SAXS. Figure 13.19 shows time course of the scattering profiles of a 12-HSA/xylene gel after quench from 55 °C (sol state) into 36 °C [74]. After crystalline nucleation occurred, i.e., (001) reflection appeared at a high  $q$  at  $t = 31.9$  s, the scattering intensity increased with keeping almost the same shape in the double logarithmic plot (Fig. 13.19b). This result suggests that the crystalline fibers grow with keeping the thickness constant.

Figure 13.19c shows a picture of a temperature-jump cell used in the time-resolved synchrotron SAXS experiments. The  $T$ -jump cell is composed of two heated blocks, where we can separately control temperature. Instantaneous temperature jump can be performed by moving the heated blocks up and down with a remote controller.

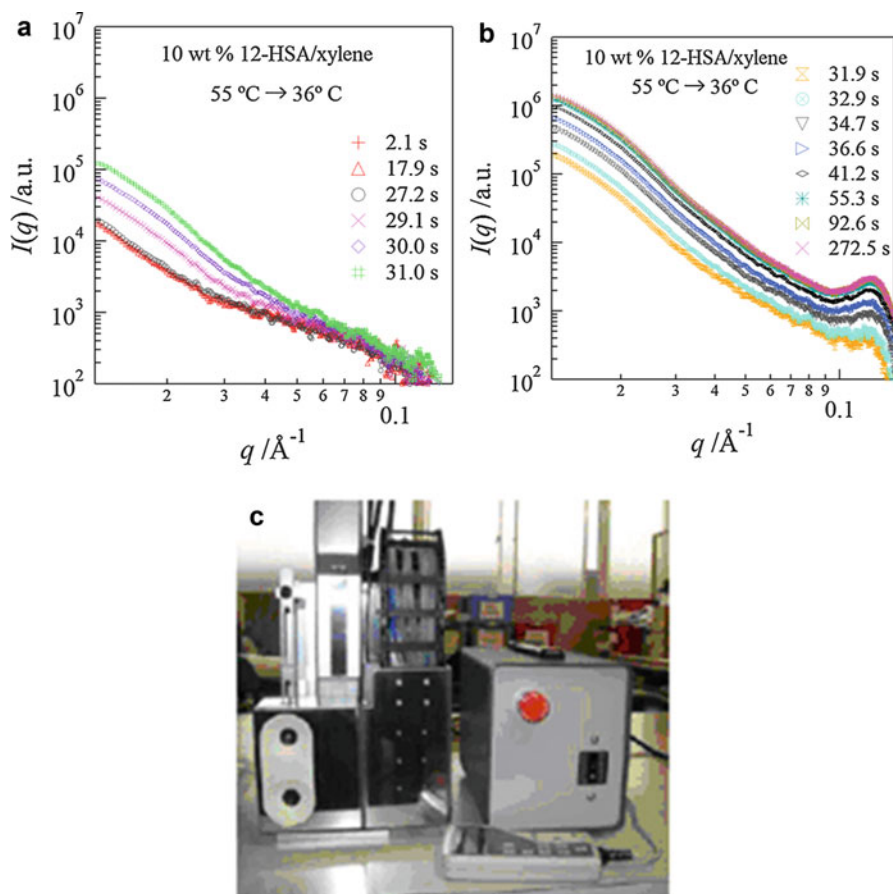


**Fig. 13.19** Time evolution of SAXS profiles for 12-HSA/xylene gel at  $36\text{ }^\circ\text{C}$  in the regime (a) before crystalline nucleation and (b) after the nucleation (Reproduced with permission from *Colloid Polym Sci* [74]. Copyright (2013) Springer, Berlin/Heidelberg) (c) Picture of a temperature-jump cell designed for synchrotron small-angle X-ray scattering

Other than  $T$ -jump and  $P$ -jump cells, various cells and apparatuses have been designed for kinetic studies of fast processes [153, 156, 157]. The various cells for studies on the dynamics of lipidic nanostructures have been summarized by a review article of Yagmur and Rappolt [157]. For crystalline polymers, polymer blends, block copolymers, and polymer gels, time-resolved SAXS and SANS have been used to pursue structural development during stretching and shear [19, 158–160]. In these studies, stress–strain curves and scattering data are simultaneously recorded.

Lund et al. designed a stopped-flow apparatus for rapid mixing and investigated the micellization kinetics of both surfactant and block copolymer micelles [153]. Figure 13.20 depicts an experimental setup with the stopped-flow apparatus (a), the time evolution of the SANS profiles after 1:1 mixing of 1.5 vol % micelle consisting

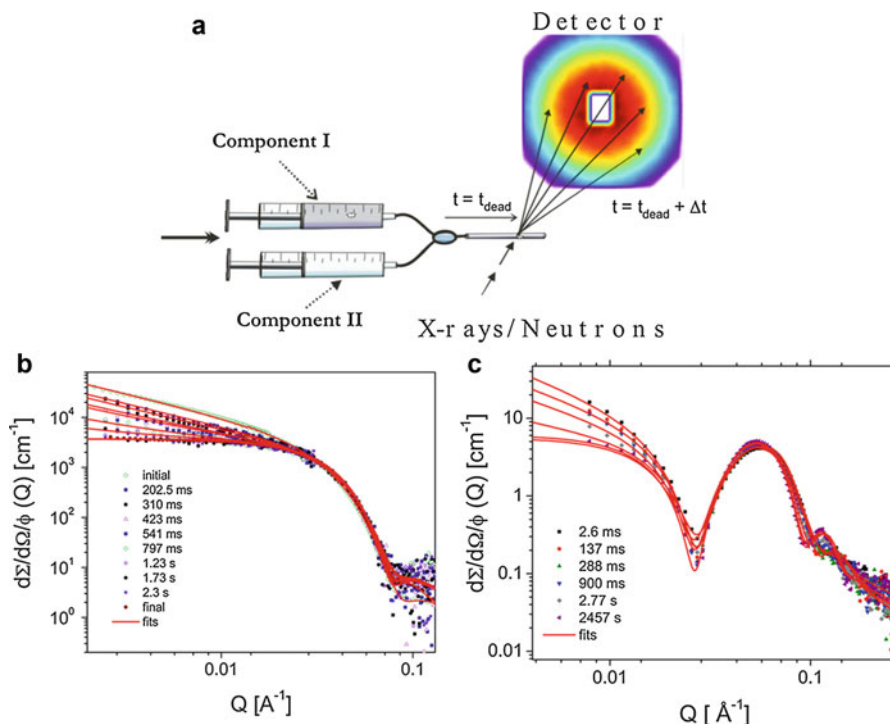


**Fig. 13.20** (a) Schematic diagram of experimental setup using a stopped-flow apparatus. (b) Time-resolved SANS data after a rapid mixing of PEP1–PEO1 in 51 % dDMF/D<sub>2</sub>O solution with pure dDMF obtained using the apparatus. (c) The time-resolved SAXS data (Reproduced with permission from *ACS Macro Letters* [153]. Copyright (2013) American Chemical Society)

of poly(ethylene-*alt*-propylene)–poly(ethylene oxide) (PEP1–PEO1) in 51 % dDMF/D<sub>2</sub>O solution with pure dDMF (b), and the time evolution of the SAXS profiles after mixing it (c) [153]. The acquisition time of the SANS measurements is 200 ms. The five repeating experiments were performed, and their data were combined. On the other hand, the acquisition time of the SAXS measurements was 5 ms with a readout time of 140 ms between two acquisitions. They observed kinetics of the cylinder-to-sphere morphological transition for the block copolymer micelle on the millisecond range using the time-resolved SAXS and SANS.

## 5.5 Complementary Utilization of SAXS and SANS

In some soft material systems, complementary use between SAXS and SANS is effective to clarify the complex structures [161–168]. In Fig. 13.20, it is interesting to notice that the shape of the SANS profiles and the SAXS profiles for PEP1–PEO1 micelle in dDMF/D<sub>2</sub>O solution is largely different, reflecting a large difference in both scattering contrasts [153]. All the SAXS intensities at various times have a



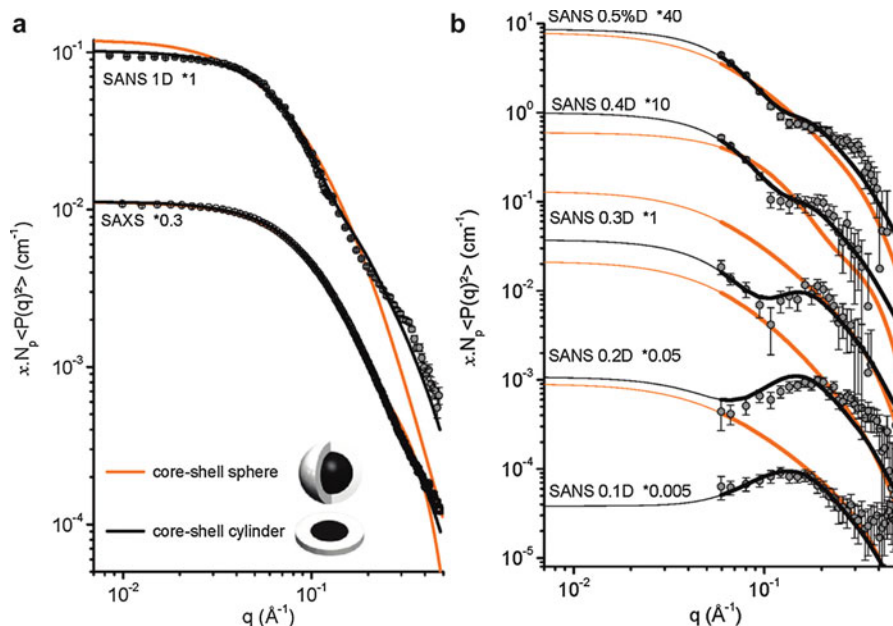


**Fig. 13.21** (a) SAXS profiles for 5 g/L asphaltene in H-toluene and SANS profiles for 5 g/L asphaltene in D-toluene. (b) Contrast variation SANS for 50 g/L asphaltene in toluene at various h/d ratios. These curves were fitted by two models of the core-shell cylinder model and the core-shell sphere model (Reproduced with permission from *J Phys Chem B* [162]. Copyright (2011) American Chemical Society)

distinct scattering peak at high  $q$  range, while all the SANS intensities at various times monotonically decrease with increasing  $q$ . This behavior is often seen for a micelle in an aqueous solution [161]. In the SANS, the scattering length density of the polymeric core makes a negative contribution, while in the SAXS it makes a positive contribution. The SANS profiles show a behavior of  $I \propto q^{-1}$  at the initial stage in a small  $q$  range, while they show a plateau-like behavior at the late stage. The former behavior indicates cylindrical-like behavior as shown in Fig. 13.4, while the latter suggests the Guinier-like behavior in the  $q$  range smaller than  $2\pi/R_g$ . Namely, these results show the cylinder-to-sphere morphological transition. On the other hand, the SAXS data show better resolution in comparison with the SANS data, although the time change in the intensity is much smaller, reflecting the small scattering contrast. Lund et al. obtained structural parameters from the fitting procedure to both SANS and SAXS data using a model of coexistence of sphere and cylindrical core-shell [153].

Eyssautier and Barre et al. performed SAXS and SANS measurements for precise structural analysis of nanoaggregates of asphaltene, which is high molecular substances in crude oil [162]. Figure 13.21 depicts (a) SAXS (5 g/L asphaltene in H-toluene) and SANS (5 g/L asphaltene in D-toluene) profiles and (b) the contrast

variation SANS (50 g/L asphaltene in toluene at various h/d ratios). Their fitting analysis shows that both models of core–shell sphere and core–shell cylinder describe their SAXS data well, i.e., it cannot be concluded from the fitting analysis which structural model is better. However, the fitting analysis of the SANS data reveals that the core–shell cylinder is the best model for asphaltene nanoaggregates. Furthermore, the contrast variation SANS clearly demonstrated that the core–shell cylinder model was superior to the core–shell sphere model.

Zemb and Diat pointed out importance of combined SAXS and SANS measurements of the same sample containing surfactants, which allow decomposition into form and structure factors [169]. Furthermore, they showed that combined SAXS and SANS measurements are useful for direct determination of the adsorption isotherm.

Complementary utilization of SAXS and SANS has been used in hard materials such as metal alloys as well as soft materials. Ohnuma et al. determined the chemical composition of the nanosized oxide in the steel matrix using the alloy contrast variation (ACV) method [166]. In both SAXS and SANS experiments, the intensity should be measured in absolute units. The chemical composition of the microstructure in the steel matrix is determined from the ratio of SAXS and SANS intensity [166, 170].

Besides, combination of small-angle scattering and other techniques such as in situ simultaneous SAXS and UV–vis, SAXS and Raman [171], simultaneous SAXS and FTIR [172], simultaneous fitting of SAXS and WAXS data [173], and combined SAXS/SANS with molecular dynamic simulations [174, 175] is also useful in addition to conventional complementary use of scattering technique and microscopy observation.

---

## 6 Conclusions and Future Perspective

In this chapter we have reviewed recent structural studies of soft materials such as polymeric micelles, low molecular weight organogels, polymer–clay nanocomposite gels, and so on. It has been shown that small-angle scattering methods such as synchrotron SAXS, USAXS, SANS, and USANS are powerful to probe structures of soft materials. Moreover, we have shown that combined scattering methods are very effective to clarify hierarchical structures. The hierarchical organization is composed of various structural levels, which depend upon the system, e.g., in the case of low molecular weight organogels, (i) spherulites, (ii) network (or fractal) structure, (iii) fibrous aggregates, (iv) cross-sectional structure of fibrous aggregates, and (v) crystalline organization in fibrous aggregates. Accompanying high performance of materials, their structures become more complicated. Therefore, it has been emphasized that sophisticated structural analysis for complex systems is indispensable. In general, however, structural analysis in multicomponent systems, e.g., that of three phases or more, becomes dramatically complex in comparison with two-phase or one-phase systems. We have shown that contrast variation SANS method using mixtures of hydrogenated and deuterated solvents with different ratios

and anomalous SAXS near the absorption edge of an element are suitable for internal structural studies of multicomponent systems. The scattering intensities measured with different scattering contrasts can be decomposed into partial structure factor of each component. The partial structure factors obtained thus presents important information on the self-correlation between nanoparticles, that between polymers, and the cross-correlation between nanoparticles and polymers.

In the future, importance of these combined methods and contrast variation methods will increase more and more with the development of high-performance materials. In practice the contrast variation SANS method introduced in this topic has been recently used for structural analysis of various high-performance materials, e.g., catalyst ink of fuel cell [118]. Anomalous SAXS may be useful for structural studies of drug delivery systems (DDS), since polymeric micelles have potential as drug carriers [176–178]. Recently, structures of polymer micelles that encapsulate drug-equivalent substances containing bromine atoms have been investigated by Sanada et al. [179]. Furthermore, anomalous X-ray scattering of light elements like sulfur and phosphorus atoms may be promising as pointed out by Stuhmann, although the experiments are technically more difficult [105]. It may be useful especially for biological systems such as nucleoproteins and membrane proteins.

**Acknowledgments** I would like to thank Prof. M. Takenaka and Dr. D. Yamaguchi for their invaluable comments and discussions. Synchrotron SAXS and SANS data in Fig. 13.3 were obtained under the approval of the Photon Factory Program Advisory Committee and under the approval of the Japan Atomic Energy Research Agency Program Advisory Committee, respectively.

---

## References

1. Guinier A, Fournet G (1955) *Small-angle scattering of X-rays*. Wiley, New York
2. Glatter O, Kratky O (1982) *Small angle X-ray scattering*. Academic, London
3. Feigin LA, Svergun DI, Taylor GW (1987) *Structure analysis by small-angle X-ray and neutron scattering*. Plenum Press, New York
4. Higgins JS, Benoît H (1994) *Polymers and neutron scattering*. Clarendon Press/Oxford University Press, Oxford/New York
5. Chu B (1997) Laser light scattering of polymer solutions. *Appl Opt* 36:7650–7656
6. Roe RJ (2000) *Methods of X-ray and neutron scattering in polymer science*. Oxford University Press, New York
7. Hammouda B (2010) SANS from polymers—review of the recent literature. *Polym Rev* 50:14–39
8. Blazek J, Gilbert EP (2011) Application of small-angle X-ray and neutron scattering techniques to the characterisation of starch structure: a review. *Carbohydr Polym* 85:281–293
9. Douch J, Gilbert EP (2013) Characterisation of large scale structures in starch granules via small-angle neutron and X-ray scattering. *Carbohydr Polym* 91:444–451
10. Boué F, Cousin F, Gummel J, Oberdisse J, El Carrot G, Harrak A (2007) Small angle scattering from soft matter—application to complex mixed systems. *C R Phys* 8:821–844
11. Dingenouts N, Bolze J, Potschke D, Ballauff M (1999) Analysis of polymer latexes by small-angle X-ray scattering. *Adv Polym Sci* 144:1–47
12. Shibayama M (2011) Small-angle neutron scattering on polymer gels: phase behavior, inhomogeneities and deformation mechanisms. *Polym J* 43:18–34

13. Guilbaud JB, Saiani A (2011) Using small angle scattering (SAS) to structurally characterise peptide and protein self-assembled materials. *Chem Soc Rev* 40:1200–1210
14. Imperor-Clerc M (2012) Three-dimensional periodic complex structures in soft matter: investigation using scattering methods. *Interface Focus* 2:589–601
15. Sears VF (1992) Neutron scattering lengths and cross sections. *Neutron News* 3:26–37
16. Stuhrmann HB (2007) Contrast variation in X-ray and neutron scattering. *J Appl Crystallogr* 40:S23–S27
17. Belushkin AV, Kozlenko DP, Rogachev AV (2011) Synchrotron and neutron-scattering methods for studies of properties of condensed matter: competition or complementarity? *J Surf Invest-X-Ray* 5:828–855
18. Shinohara Y, Kishimoto H, Inoue K, Suzuki Y, Takeuchi A, Uesugi K, Yagi N, Muraoka K, Mizoguchi T, Amemiya Y (2007) Characterization of two-dimensional ultra-small-angle X-ray scattering apparatus for application to rubber filled with spherical silica under elongation. *J Appl Crystallogr* 40:S397–S401
19. Takeno H, Uehara H, Murakami S, Takenaka M, Kim MI, Nagasawa N, Sasaki S (2007) Structural development of dynamically asymmetric polymer blends under uniaxial stretching. *J Appl Crystallogr* 40:S656–S661
20. Takeno H, Obuchi K, Maki Y, Kondo S, Dobashi T (2011) A structural study of polyelectrolyte gels in a unidirectionally swollen state. *Polymer* 52:2685–2692
21. Paww BR (2013) Everything SAXS: small-angle scattering pattern collection and correction. *J Phys Condens Matter* 25:383201
22. Paww BR (2014) Corrigendum: Everything SAXS: small-angle scattering pattern collection and correction (2013 *J Phys Condens Matter* 25:383201). *J Phys Condens Matter* 26:239501
23. Kline SR (2006) Reduction and analysis of SANS and USANS data using IGOR Pro. *J Appl Crystallogr* 39:895–900
24. Ilavsky J, Jemian PR (2009) Irena: tool suite for modeling and analysis of small-angle scattering. *J Appl Crystallogr* 42:347–353
25. Spinozzi F, Ferrero C, Ortore MG, Antolinos AD, Mariani P (2014) GENFIT: software for the analysis of small-angle X-ray and neutron scattering data of macromolecules in solution. *J Appl Crystallogr* 47:1132–1139
26. Kaneko F, Seto N, Sasaki K, Sakurai S, Kimura T (2013) Simultaneous SAXS and WAXS study on the guest exchange process of syndiotactic polystyrene: crystalline complex formation with triethylene glycol dimethyl ether. *Macromol Chem Phys* 214:1893–1900
27. Portale G, Cavallo D, Alfonso GC, Hermida-Merino D, van Drongelen M, Balzano L, Peters GWM, Goossens JGP, Bras W (2013) Polymer crystallization studies under processing-relevant conditions at the SAXS/WAXS DUBBLE beamline at the ESRF. *J Appl Crystallogr* 46:1681–1689
28. Tolentino A, León S, Alla A, Martínez de Ilarduya A, Muñoz-Guerra S (2013) The structure of poly( $\gamma$ -glutamic acid)/nanoclay hybrids compatibilized by alkylammonium surfactants. *Eur Polym J* 49:2596–2609
29. Liu G, Schneider K, Zheng L, Zhang X, Li C, Stamm M, Wang D (2014) Stretching induced phase separation in poly(vinylidene fluoride)/poly(butylene succinate) blends studied by in-situ X-ray scattering. *Polymer* 55:2588–2596
30. Rath T, Novák J, Amenitsch H, Pein A, Maier E, Haas W, Hofer F, Trimmel G (2014) Real time X-ray scattering study of the formation of ZnS nanoparticles using synchrotron radiation. *Mater Chem Phys* 144:310–317
31. Bonse U, Hart M (1965) Tailless X-ray single-crystal reflection curves obtained by multiple reflection – (Si Ge crystals – E/T). *Appl Phys Lett* 7:238
32. Koga T, Hart M, Hashimoto T (1996) Development of a high-flux- and high-temperature-set-up Bonse-Hart ultra-small-angle X-ray scattering (USAXS) diffractometer. *J Appl Crystallogr* 29:318–324
33. Chaboussant G, Désert S, Brület A (2012) Recent developments and projects in SANS instrumentation at LLB-Orphée. *Eur Phys J Spec Top* 213:313–325

34. Dewhurst CD (2014) Novel multiple-beam very small angle neutron scattering (VSANS) using a conventional SANS instrument. *J Appl Crystallogr* 47:1180–1189
35. Freelon B, Suthar K, Ilavsky J (2013) A multi-length-scale USAXS/SAXS facility: 10–50 keV small-angle X-ray scattering instrument. *J Appl Crystallogr* 46:1508–1512
36. Ilavsky J, Jemian PR, Allen AJ, Zhang F, Levine LE, Long GG (2009) Ultra-small-angle X-ray scattering at the advanced photon source. *J Appl Crystallogr* 42:469–479
37. Koizumi S, Iwase H, Suzuki J, Oku T, Motokawa R, Sasao H, Tanaka H, Yamaguchi D, Shimizu HM, Hashimoto T (2006) Focusing and polarized neutron ultra-small-angle scattering spectrometer (SANS-J-II) at Research Reactor JRR3, Japan. *Phys B Condens Matter* 385–86:1000–1006
38. Koizumi S, Iwase H, Suzuki JI, Oku T, Motokawa R, Sasao H, Tanaka H, Yamaguchi D, Shimizu HM, Hashimoto T (2007) Focusing and polarized neutron small-angle scattering spectrometer (SANS-J-II). The challenge of observation over length scales from an angstrom to a micrometre. *J Appl Crystallogr* 40:S474–S479
39. Rehm C, Barker J, Bouwman WG, Pynn R (2013) DCD USANS and SESANS: a comparison of two neutron scattering techniques applicable for the study of large-scale structures. *J Appl Crystallogr* 46:354–364
40. Rehm C, Brule A, Freund AK, Kennedy SJ (2013) Kookaburra: the ultra-small-angle neutron scattering instrument at OPAL. *J Appl Crystallogr* 46:1699–1704
41. Sztucki M, Narayanan T (2007) Development of an ultra-small-angle X-ray scattering instrument for probing the microstructure and the dynamics of soft matter. *J Appl Crystallogr* 40: S459–S462
42. Zhang F, Ilavsky J (2010) Ultra-small-angle X-ray scattering of polymers. *Polym Rev* 50:59–90
43. Takenaka M (2013) Analysis of structures of rubber-filler systems with combined scattering methods. *Polym J* 45:10–19
44. Weiss RG (2014) The past, present, and future of molecular gels. What is the status of the field, and where is it going? *J Am Chem Soc* 136:7519–7530
45. Weiss RG, Terech P (2006) *Molecular gels materials with self-assembled fibrillar networks*. Springer, Dordrecht
46. Takeno H, Maehara A, Kuchiishi M, Yoshiba K, Takeshita H, Kondo S, Dobashi T, Takenaka M, Hasegawa H (2012) Structural and thermal properties of unpurified and purified 12-hydroxystearic acid solutions. *Sen'i Gakkaishi* 68:248–252
47. Takeno H, Mochizuki T, Yoshiba K, Kondo S, Dobashi T (2009) Self-assembling structures and sol–gel transition of optically active and racemic 12-hydroxystearic acids in organic solvents. *Progr Colloid Polym Sci* 136:47–53
48. Takeno H, Maehara A, Yamaguchi D, Koizumi S (2012) A structural study of an organogel investigated by small-angle neutron scattering and synchrotron small-angle X-ray scattering. *J Phys Chem B* 116:7739–7745
49. Liu XY, Sawant PD (2001) Formation kinetics of fractal nanofiber networks in organogels. *Appl Phys Lett* 79:3518–3520
50. Liu XY, Sawant PD (2002) Mechanism of the formation of self-organized microstructures in soft functional materials. *Adv Mater* 14:421–426
51. Koga T, Hashimoto T, Takenaka M, Aizawa K, Amino N, Nakamura M, Yamaguchi D, Koizumi S (2008) New insight into hierarchical structures of carbon black dispersed in polymer matrices: a combined small-angle scattering study. *Macromolecules* 41:453–464
52. Takenaka M, Nishitsuji S, Amino N, Ishikawa Y, Yamaguchi D, Koizumi S (2009) Structure analyses of swollen rubber-filler systems by using contrast variation SANS. *Macromolecules* 42:308–311
53. Takenaka M, Nishitsuji S, Amino N, Ishikawa Y, Yamaguchi D, Koizumi S (2012) Structure analyses of swollen rubber-carbon black systems by using contrast variation small-angle neutron scattering. *Rubber Chem Technol* 85:157–164

54. Hashimoto T (2004) Small-angle neutron scattering studies of dynamics and hierarchical pattern formation in binary mixtures of polymers and small molecules. *J Polym Sci Pol Phys* 42:3027–3062
55. Schaefer DW, Rieker T, Agamalian M, Lin JS, Fischer D, Sukumaran S, Chen CY, Beaucage G, Herd C, Ivie J (2000) Multilevel structure of reinforcing silica and carbon. *J Appl Crystallogr* 33:587–591
56. Iwase H, S-i S, Yamaki T, Koizumi S, Ohnuma M, Maekawa Y (2012) Hierarchical structure analysis of graft-type polymer electrolyte membranes consisting of cross-linked polytetrafluoroethylene by small-angle scattering in a wide-Q range. *Macromolecules* 45:9121–9127
57. Allen AJ (2005) Characterization of ceramics by X-ray and neutron small-angle scattering. *J Am Ceram Soc* 88:1367–1381
58. Hashimoto T (2012) Combined small-angle scattering analysis of hierarchically self-assembled soft matters: unique “sponge-like” gel structure as an example of dissipative patterns formed in open non-equilibrium systems. *Chin J Phys* 50:171–192
59. Kroon M, Vos WL, Wegdam GH (1998) Structure and formation of a gel of colloidal disks. *Phys Rev E* 57:1962–1970
60. Pignon F, Magnin A, Piau JM, Cabane B, Lindner P, Diat O (1997) Yield stress thixotropic clay suspension: investigation of structure by light, neutron, and x-ray scattering. *Phys Rev E* 56:3281–3289
61. Hashimoto T, Koizumi S (2012) *Polymer science: a comprehensive reference*. Elsevier, Amsterdam
62. Tanaka H, Koizumi S, Hashimoto T, Kurosaki K, Kobayashi S (2007) Self-assembly of synthetic cellulose during in-vitro enzymatic polymerization process as studied by a combined small-angle scattering method. *Macromolecules* 40:6304–6315
63. Beaucage G (1995) Approximations leading to a unified exponential power-law approach to small-angle scattering. *J Appl Crystallogr* 28:717–728
64. Beaucage G (1996) Small-angle scattering from polymeric mass fractals of arbitrary mass-fractal dimension. *J Appl Crystallogr* 29:134–146
65. Beaucage G (2004) Determination of branch fraction and minimum dimension of mass-fractal aggregates. *Phys Rev E* 70:031401
66. Beaucage G, Schaefer DW (1994) Structural studies of complex-systems using small-angle scattering – a unified Guinier power-law approach. *J Non-Cryst Solids* 172:797–805
67. Beaucage G, Kammler HK, Pratsinis SE (2004) Particle size distributions from small-angle scattering using global scattering functions. *J Appl Crystallogr* 37:523–535
68. Mihara S, Datta RN, Dierkes WK, Noordermeer JWM, Amino N, Ishikawa Y, Nishitsuji S, Takenaka M (2014) Ultra small-angle X-ray scattering study of flocculation in silica-filled rubber. *Rubber Chem Technol* 87:348–359
69. Papagiannopoulos A, Zhao J, Zhang G, Pispas S, Radulescu A (2014) Thermoresponsive aggregation of PS–PNIPAM–PS triblock copolymer: a combined study of light scattering and small angle neutron scattering. *Eur Polym J* 56:59–68
70. Hammouda B (2010) Analysis of the Beaucage model. *J Appl Crystallogr* 43:1474–1478
71. Hammouda B (2010) A new Guinier–Porod model. *J Appl Crystallogr* 43:716–719
72. Kotlarchyk M, Chen SH (1983) Analysis of small-angle neutron-scattering spectra from polydisperse interacting colloids. *J Chem Phys* 79:2461–2469
73. Abreu MF, dos Santos DR, Gatts CEN, Giacomini R, Cardoso SL, Miranda PCML (2014) Small-angle X-ray scattering structural study of the nanofiber self-assembly process in supra-molecular gels based on glucopyranosides. *J Appl Crystallogr* 47:1284–1297
74. Takeno H, Mochizuki T (2013) A structural development of an organogel explored by synchrotron time-resolved small-angle X-ray scattering. *Colloid Polym Sci* 291:2783–2789
75. Takeno H, Kuribayashi Y (2015) A synchrotron small-angle X-ray scattering study on structures of 1,3:2,4-dibenzylidene sorbitol gels. *Colloid Surf A* 467:173–179
76. Mittelbach P, Porod G (1961) Zur Röntgenklein winkelstreuung verdünnter kolloider Systeme. Die Berechnung der Streukurven von Parallelepiped. *Acta Phys Austriaca* 14:185–211

77. Lee HY, Oh H, Lee JH, Raghavan SR (2012) Shedding light on helical microtubules: real-time observations of microtubule self-assembly by light microscopy. *J Am Chem Soc* 134:14375–14381
78. Li Y, Li B, Fu Y, Lin S, Yang Y (2013) Solvent-induced handedness inversion of dipeptide sodium salts derived from alanine. *Langmuir* 29:9721–9726
79. Terech P, SKP V, Pernot P, Wiegart L (2012) Salt effects in the formation of self-assembled lithocholate helical ribbons and tubes. *J Phys Chem B* 116:11344–11355
80. Ziserman L, Lee HY, Raghavan SR, Mor A, Danino D (2011) Unraveling the mechanism of nanotube formation by chiral self-assembly of amphiphiles. *J Am Chem Soc* 133: 2511–2517
81. Pringle OA, Schmidt PW (1971) Small-angle X-ray scattering from helical macromolecules. *J Appl Crystallogr* 4:290–293
82. Teixeira CV, Amenitsch H, Fukushima T, Hill JP, Jin W, Aida T, Hotokka M, Lindén M (2010) Form factor of an N-layered helical tape and its application to nanotube formation of hexa-peri-hexabenzocoronene-based molecules. *J Appl Crystallogr* 43:850–857
83. Terech P, Volino F, Ramasseul R (1985) Small-angle neutron-scattering study of steroidal gels. *J Phys Paris* 46:895–903
84. Hamley IW (2008) Form factor of helical ribbons. *Macromolecules* 41:8948–8950
85. de Gennes P-G (1979) *Scaling concepts in polymer physics*. Cornell University Press, Ithaca/London
86. Takeno H, Koizumi S, Hasegawa H, Hashimoto T (1996) Small-angle neutron scattering study of anomalous mixing behaviors in deuterated polystyrene poly(vinyl methyl ether) mixtures near the glass transition temperature. *Macromolecules* 29:2440–2448
87. Takeno H, Kuribayashi Y (2014) Structural studies of 1,3:2,4-dibenzylidene sorbitol gels. *Adv Mater Res* 896:300–304
88. Takeno H, Yanagita M, Motegi Y, Kondo S (2015) Relationship between helical aggregates and polymorphs in a 12-hydroxystearic acid gel: their thermal stability and formation kinetics. *Colloid Polym Sci* 293:199–207
89. Takeno H, Koizumi S (2006) Incoherent neutron scattering study on the local dynamics in polystyrene and poly(vinyl methyl ether) blends. *Polymer* 47:5946–5951
90. Long B, Chodakowski M, Shaw JM (2013) Impact of liquid–vapor to liquid–liquid–vapor phase transitions on asphaltene-rich nanoaggregate behavior in athabasca vacuum residue + pentane mixtures. *Energy Fuel* 27:1779–1790
91. Pattier B, Henderson M, Brotons G, Gibaud A (2010) Study of titanium oxide sol–gel condensation using small angle X-ray scattering. *J Phys Chem B* 114:5227–5232
92. Hollamby MJ, Borisova D, Brown P, Eastoe J, Grillo I, Shchukin D (2012) Growth of mesoporous silica nanoparticles monitored by time-resolved small-angle neutron scattering. *Langmuir* 28:4425–4433
93. Johansen D, Jeffries CM, Hammouda B, Trehwella J, Goldenberg DP (2011) Effects of macromolecular crowding on an intrinsically disordered protein characterized by small-angle neutron scattering with contrast matching. *Biophys J* 100:1120–1128
94. Jouault N, Dalmas F, Said S, Di Cola E, Schweins R, Jestin J, Boue F (2010) Direct measurement of polymer chain conformation in well-controlled model nanocomposites by combining SANS and SAXS. *Macromolecules* 43:9881–9891
95. Nusser K, Neueder S, Schneider GJ, Meyer M, Pyckhout-Hintzen W, Willner L, Radulescu A, Richter D (2010) Conformations of silica-poly(ethylene-propylene) nanocomposites. *Macromolecules* 43:9837–9847
96. Sharma KP, Aswal VK, Kumaraswamy G (2010) Adsorption of nonionic surfactant on silica nanoparticles: structure and resultant interparticle interactions. *J Phys Chem B* 114:10986–10994
97. Shibayama M, Karino T, Miyazaki S, Okabe S, Takehisa T, Haraguchi K (2005) Small-angle neutron scattering study on uniaxially stretched poly(N-isopropylacrylamide)-clay nanocomposite gels. *Macromolecules* 38:10772–10781

98. Avdeev MV (2007) Contrast variation in small-angle scattering experiments on polydisperse and superparamagnetic systems: basic functions approach. *J Appl Crystallogr* 40:56–70
99. Endo H (2006) Study on multicomponent systems by means of contrast variation SANS. *Phys B Condens Matter* 385:682–684
100. Endo H, Schwahn D, Colfen H (2004) On the role of block copolymer additives for calcium carbonate crystallization: small angle neutron scattering investigation by applying contrast variation. *J Chem Phys* 120:9410–9423
101. Miyazaki S, Endo H, Karino T, Haraguchi K, Shibayama M (2007) Gelation mechanism of poly(N-isopropylacrylamide)-clay nanocomposite gels. *Macromolecules* 40:4287–4295
102. Dingenouts N, Ballauff M (1993) Small-angle X-ray-analysis of latex-particles using contrast variation. *Acta Polym* 44:178–183
103. Hickl P, Ballauff M, Jada A (1996) Small-angle X-ray contrast-variation study of micelles formed by poly(styrene)-poly(ethylene oxide) block copolymers in aqueous solution. *Macromolecules* 29:4006–4014
104. Naruse K, Eguchi K, Akiba I, Sakurai K, Masunaga H, Ogawa H, Fossey JS (2009) Flexibility and cross-sectional structure of an anionic dual-surfactant wormlike micelle explored with small-angle X-ray scattering coupled with contrast variation technique. *J Phys Chem B* 113:10222–10229
105. Stuhmann HB (2008) Small-angle scattering and its interplay with crystallography, contrast variation in SAXS and SANS. *Acta Crystallogr A* 64:181–191
106. Akiba I, Takechi A, Sakou M, Handa M, Shinohara Y, Amemiya Y, Yagi N, Sakurai K (2012) Anomalous small-angle X-ray scattering study of structure of polymer micelles having bromines in hydrophobic core. *Macromolecules* 45:6150–6157
107. Dingenouts N, Patel M, Rosenfeldt S, Pontoni D, Narayanan T, Ballauff M (2004) Counterion distribution around a spherical polyelectrolyte brush probed by anomalous small-angle X-ray scattering. *Macromolecules* 37:8152–8159
108. Lee B, Lo CT, Seifert S, Rago NLD, Winans RE, Thiyagarajan P (2007) Anomalous small-angle X-ray scattering characterization of bulk block copolymer/nanoparticle composites. *Macromolecules* 40:4235–4243
109. Pabit SA, Finkelstein KD, Pollack L (2009) Using anomalous small angle X-ray scattering to probe the ion atmosphere around nucleic acids. *Methods Enzymol* 469:391–410
110. Sztucki M, Di Cola E, Narayanan T (2012) Anomalous small-angle X-ray scattering from charged soft matter. *Eur Phys J Spec Top* 208:319–331
111. Thiyagarajan P (2003) Characterization of materials of industrial importance using small-angle scattering techniques. *J Appl Crystallogr* 36:373–380
112. Chevigny C, Jestin J, Gignes D, Schweins R, Di-Cola E, Dalmas F, Bertin D, Boue F (2010) “Wet-to-dry” conformational transition of polymer layers grafted to nanoparticles in nanocomposite. *Macromolecules* 43:4833–4837
113. Suzuki T, Endo H, Shibayama M (2008) Analysis of surface structure and hydrogen/deuterium exchange of colloidal silica suspension by contrast-variation small-angle neutron scattering. *Langmuir* 24:4537–4543
114. Chevigny C, Gignes D, Bertin D, Jestin J, Boue F (2009) Polystyrene grafting from silica nanoparticles via nitroxide-mediated polymerization (NMP): synthesis and SANS analysis with the contrast variation method. *Soft Matter* 5:3741–3753
115. Endo H, Mihailescu M, Monkenbusch M, Allgaier J, Gompper G, Richter D, Jakobs B, Sottmann T, Strey RIG (2001) Effect of amphiphilic block copolymers on the structure and phase behavior of oil–water-surfactant mixtures. *J Chem Phys* 115:580–600
116. Matsunaga T, Endo H, Takeda M, Shibayama M (2010) Microscopic structure analysis of clay-poly(ethylene oxide) mixed solution in a flow field by contrast-variation small-angle neutron scattering. *Macromolecules* 43:5075–5082
117. Nishida T, Endo H, Osaka N, Li H, Haraguchi K, Shibayama M (2009) Deformation mechanism of nanocomposite gels studied by contrast variation small-angle neutron scattering. *Phys Rev E* 80:030801



118. Shibayama M, Matsunaga T, Kusano T, Amemiya K, Kobayashi N, Yoshida T (2014) SANS studies on catalyst ink of fuel cell. *J Appl Polym Sci* 131:39842
119. Rose S, Dizeux A, Narita T, Hourdet D, Marcellan A (2013) Time dependence of dissipative and recovery processes in nanohybrid hydrogels. *Macromolecules* 46:4095–4104
120. Shibayama M, Suda J, Karino T, Okabe S, Takehisa T, Haraguchi K (2004) Structure and dynamics of poly(N-isopropylacrylamide)-clay nanocomposite gel. *Macromolecules* 37:9606–9612
121. Shinohara Y, Kishimoto H, Yagi N, Amemiya Y (2010) Microscopic observation of aging of silica particles in unvulcanized rubber. *Macromolecules* 43:9480–9487
122. Potts JR, Dreyer DR, Bielawski CW, Ruoff RS (2011) Graphene-based polymer nanocomposites. *Polymer* 52:5–25
123. Yoonessi M, Gaier JR (2010) Highly conductive multifunctional graphene polycarbonate nanocomposites. *ACS Nano* 4:7211–7220
124. Haraguchi K, Li HJ, Matsuda K, Takehisa T, Elliott E (2005) Mechanism of forming organic/inorganic network structures during in-situ free-radical polymerization in PNIPAA-clay nanocomposite hydrogels. *Macromolecules* 38:3482–3490
125. Haraguchi K, Takehisa T, Fan S (2002) Effects of clay content on the properties of nanocomposite hydrogels composed of poly(N-isopropylacrylamide) and clay. *Macromolecules* 35:10162–10171
126. Haraguchi K, Uyama K, Tanimoto H (2011) Self-healing in nanocomposite hydrogels. *Macromol Rapid Commun* 32:1253–1258
127. Okay O, Oppermann W (2007) Polyacrylamide-clay nanocomposite hydrogels: rheological and light scattering characterization. *Macromolecules* 40:3378–3387
128. Ren HY, Zhu M, Haraguchi K (2011) Characteristic swelling-deswelling of polymer/clay nanocomposite gels. *Macromolecules* 44:8516–8526
129. Wang Q, Mynar JL, Yoshida M, Lee E, Lee M, Okuro K, Kinbara K, Aida T (2010) High-water-content mouldable hydrogels by mixing clay and a dendritic molecular binder. *Nature* 463:339–343
130. Takeno H, Nakamura W (2013) Structural and mechanical properties of composite hydrogels composed of clay and a polyelectrolyte prepared by mixing. *Colloid Polym Sci* 291:1393–1399
131. Endo H, Miyazaki S, Haraguchi K, Shibayama M (2008) Structure of nanocomposite hydrogel investigated by means of contrast variation small-angle neutron scattering. *Macromolecules* 41:5406–5411
132. Varga Z, Bota A, Goerigk G (2006) Localization of dibromophenol in DPPC/water liposomes studied by anomalous small-angle X-ray scattering. *J Phys Chem B* 110:11029–11032
133. Stuhrmann HB (1985) Resonance scattering in macromolecular structure research. *Adv Polym Sci* 67:123–163
134. Goerigk G, Huber K, Mattern N, Williamson DL (2012) Quantitative anomalous small-angle X-ray scattering—the determination of chemical concentrations in nano-scaled phases. *Eur Phys J Spec Top* 208:259–274
135. Barnardo T, Hoydalsvik K, Winter R, Martin CM, Clark GF (2009) In situ double anomalous small-angle X-ray scattering of the sintering and calcination of sol-gel prepared yttria-stabilized-zirconia ceramics. *J Phys Chem C* 113:10021–10028
136. Bota A, Goerigk G, Drucker T, Haubold HG, Petro J (2002) Anomalous small-angle X-ray scattering on a new, nonpyrophoric Raney-type Ni catalyst. *J Catal* 205:354–357
137. Okuda H, Fukumoto T, Saida J, Ochiai S, Sasaki S, Masunaga H (2008) Anomalous small-angle scattering from nanoquasicrystalline precipitates in Zr80Pt20 ribbons. *J Appl Crystallogr* 41:675–679
138. Polizzi S, Riello P, Goerigk G, Benedetti A (2002) Quantitative investigations of supported metal catalysts by ASAXS. *J Synchrotron Radiat* 9:65–70
139. Rasmussen FB, Molenbroek AM, Clausen BS, Feidenhans R (2000) Particle size distribution of a Ni/SiO<sub>2</sub> catalyst determined by ASAXS. *J Catal* 190:205–208

140. Pabit SA, Meisburger SP, Li L, Blose JM, Jones CD, Pollack L (2010) Counting ions around DNA with anomalous small-angle X-ray scattering. *J Am Chem Soc* 132:16334–16336
141. Sakou M, Takechi A, Handa M, Shinohara Y, Amemiya Y, Masunaga H, Ogawa H, Yagi N, Sakurai K, Akiba I (2011) Anomalous small-angle X-ray scattering study on aggregation of a block copolymer in a selective solvent. *J Phys Conf Ser* 272:012022
142. Varga Z, Berenyi S, Szokol B, Orfi L, Keri G, Petak I, Hoell A, Bota A (2010) A closer look at the structure of sterically stabilized liposomes: a small-angle X-ray scattering study. *J Phys Chem B* 114:6850–6854
143. Goerigk G, Mattern N (2010) Spinodal decomposition in Ni-Nb-Y metallic glasses analyzed by quantitative anomalous small-angle X-ray scattering. *J Phys Conf Ser* 247:012022
144. Gutsche A, Daikeler A, Guo X, Dingenouts N, Nirschl H (2014) Time-resolved SAXS characterization of the shell growth of silica-coated magnetite nanocomposites. *J Nanoparticle Res* 16:2475
145. Yan S, Wu Z, Yu H, Gong Y, Tan Y, Du R, Chen W, Xing X, Mo G, Chen Z, Cai Q, Sun D (2014) Time-resolved small-angle X-ray scattering study on the growth behavior of silver nanoparticles. *J Phys Chem C* 118:11454–11463
146. Adelsberger J, Metwalli E, Diethert A, Grillo I, Bivigou-Koumba AM, Laschewsky A, Müller-Buschbaum P, Papadakis CM (2012) Kinetics of collapse transition and cluster formation in a thermoresponsive micellar solution of P(S-b-NIPAM-b-S) induced by a temperature jump. *Macromol Rapid Commun* 33:254–259
147. Lu J, Bates FS, Lodge TP (2013) Chain exchange in binary copolymer micelles at equilibrium: confirmation of the independent chain hypothesis. *ACS Macro Lett* 2:451–455
148. Nishi K, Asai H, Fujii K, Han Y-S, Kim T-H, Sakai T, Shibayama M (2014) Small-angle neutron scattering study on defect-controlled polymer networks. *Macromolecules* 47:1801–1809
149. Takenaka M, Takeno H, Hasegawa H, Saito S, Hashimoto T, Nagao M (2002) Viscoelastic effects in relaxation processes of concentration fluctuations in dynamically asymmetric polymer blends. *Phys Rev E* 65:021806
150. Takenaka M, Takeno H, Hashimoto T, Nagao M (2003) Viscoelastic effects in dynamics of concentration fluctuations in dynamically asymmetric polymer blends. *J Appl Crystallogr* 36:642–645
151. Takenaka M, Takeno H, Hashimoto T, Nagao M (2006) Viscoelastic effects on early stage of spinodal decomposition in dynamically asymmetric polymer blends. *J Chem Phys* 124:104904
152. Kyriakos K, Philipp M, Adelsberger J, Jaksch S, Berezkin AV, Lugo DM, Richtering W, Grillo I, Miasnikova A, Laschewsky A, Müller-Buschbaum P, Papadakis CM (2014) Cononsolvency of water/methanol mixtures for PNIPAM and PS-b-PNIPAM: pathway of aggregate formation investigated using time-resolved SANS. *Macromolecules* 47:6867–6879
153. Lund R, Willner L, Richter D, Lindner P, Narayanan T (2013) Kinetic pathway of the cylinder-to-sphere transition in block copolymer micelles observed in situ by time-resolved neutron and synchrotron scattering. *ACS Macro Lett* 2:1082–1087
154. Takenaka M, Miyazawa M, Miyajima T, Hashimoto T (2005) Synchrotron small-angle X-ray scattering of relaxation process in a nontangled diblock copolymer. *Macromolecules* 38:8481–8485
155. Takeno H, Nagao M, Nakayama Y, Hasegawa H, Hashimoto T, Seto H, Imai M (1997) High pressure cell for small-angle neutron and light scattering studies of phase transitions in complex liquids. *Polym J* 29:931–939
156. Blazek J, Gilbert EP (2010) Effect of enzymatic hydrolysis on native starch granule structure. *Biomacromolecules* 11:3275–3289
157. Yagmur A, Rappolt M (2012) Structural characterization of lipidic systems under nonequilibrium conditions. *Eur Biophys J* 41:831–840
158. Mao Y, Burger C, Li X, Hsiao BS, Mehta AK, Tsou AH (2012) Time-resolved synchrotron X-ray scattering study on propylene-1-butylene random copolymer subjected to uniaxial stretching at high temperatures. *Macromolecules* 45:951–961

159. Meins T, Hyun K, Dingenouts N, Fotouhi Ardakani M, Struth B, Wilhelm M (2012) New insight to the mechanism of the shear-induced macroscopic alignment of diblock copolymer melts by a unique and newly developed Rheo-SAXS combination. *Macromolecules* 45:455–472
160. Stribeck N, Zeinolebadi A, Ganjaee Sari M, Botta S, Jankova K, Hvilsted S, Drozdov A, Klitkou R, Potarniche C-G, Christiansen JD, Ermini V (2012) Properties and semicrystalline structure evolution of polypropylene/montmorillonite nanocomposites under mechanical load. *Macromolecules* 45:962–973
161. Arleth L, Ashok B, Onyuksel H, Thiyagarajan P, Jacob J, Hjelm RP (2005) Detailed structure of hairy mixed micelles formed by phosphatidylcholine and PEGylated phospholipids in aqueous media. *Langmuir* 21:3279–3290
162. Ji E, Levitz P, Espinat D, Jestin J, Jrm G, Grillo I, Lc B (2011) Insight into asphaltene nanoaggregate structure inferred by small angle neutron and X-ray scattering. *J Phys Chem B* 115:6827–6837
163. Hirai M (2007) Feasibility of complementary use of neutron and X-ray scattering techniques in research of lipid mixtures. *J Phys Conf Ser* 83:012003
164. Motokawa R, Suzuki S, Ogawa H, Antonio MR, Yaita T (2012) Microscopic structures of tri-n-butyl phosphate/n-octane mixtures by X-ray and neutron scattering in a wide q range. *J Phys Chem B* 116:1319–1327
165. Ogino Y, Fukushima H, Matsuba G, Takahashi N, Nishida K, Kanaya T (2006) Effects of high molecular weight component on crystallization of polyethylene under shear flow. *Polymer* 47:5669–5677
166. Ohnuma M, Suzuki J, Ohtsuka S, Kim SW, Kaito T, Inoue M, Kitazawa H (2009) A new method for the quantitative analysis of the scale and composition of nanosized oxide in 9Cr-ODS steel. *Acta Mater* 57:5571–5581
167. Schmiele M, Schindler T, Westermann M, Steiniger F, Radulescu A, Kriele A, Gilles R, Unruh T (2014) Mesoscopic structures of triglyceride nanosuspensions studied by small-angle X-ray and neutron scattering and computer simulations. *J Phys Chem B* 118:8808–8818
168. Sun YS, Jeng US, Huang YS, Liang KS, Lin TL, Tsao CS (2006) Complementary SAXS and SANS for structural characteristics of a polyurethane elastomer of low hard-segment content. *Phys B Condens Matter* 385:650–652
169. Zemb T, Diat O (2010) What can we learn from combined SAXS and SANS measurements of the same sample containing surfactants? *J Phys Conf Ser* 247:012002
170. Oba Y, Koppoju S, Ohnuma M, Kinjo Y, Morooka S, Tomota Y, Suzuki J, Yamaguchi D, Koizumi S, Sato M, Shiraga T (2012) Quantitative analysis of inclusions in low carbon free cutting steel using small-angle X-ray and neutron scattering. *ISIJ Int* 52:457–463
171. Haas S, Plivelic TS, Dicko C (2014) Combined SAXS/UV-vis/Raman as a diagnostic and structure resolving tool in materials and life sciences applications. *J Phys Chem B* 118:2264–2273
172. Ratri PJ, Tashiro K (2013) Application of the simultaneous measurement system of WAXD, SAXS and transmission FTIR spectra to the study of structural changes in the cold- and melt-crystallization processes of trans-1,4-polyisoprene. *Polym J* 45:1019–1026
173. Gagin A, Allen AJ, Levin I (2014) Combined fitting of small- and wide-angle X-ray total scattering data from nanoparticles: benefits and issues. *J Appl Crystallogr* 47:619–629
174. Eremin RA, Kholmurodov K, Petrenko VI, Rosta L, Avdeev MV (2013) Effect of the solute-solvent interface on small-angle neutron scattering from organic solutions of short alkyl chain molecules as revealed by molecular dynamics simulation. *J Appl Crystallogr* 46:372–378
175. McDermott AG, Larsen GS, Budd PM, Colina CM, Runt J (2011) Structural characterization of a polymer of intrinsic microporosity: X-ray scattering with interpretation enhanced by molecular dynamics simulations. *Macromolecules* 44:14–16
176. Matsumura Y, Kataoka K (2009) Preclinical and clinical studies of anticancer agent-incorporating polymer micelles. *Cancer Sci* 100:572–579

177. Yang YQ, Zhao B, Li ZD, Lin WJ, Zhang CY, Guo XD, Wang JF, Zhang LJ (2013) pH-sensitive micelles self-assembled from multi-arm star triblock co-polymers poly(epsilon-caprolactone)-b-poly(2-(diethylamino)ethyl methacrylate)-b-poly(poly(ethylene glycol) methyl ether methacrylate) for controlled anticancer drug delivery. *Acta Biomater* 9:7679–7690
178. Yang YQ, Zheng LS, Guo XD, Qian Y, Zhang LJ (2011) pH-sensitive micelles self-assembled from amphiphilic copolymer brush for delivery of poorly water-soluble drugs. *Biomacromolecules* 12:116–122
179. Sanada Y, Akiba I, Sakurai K, Shiraishi K, Yokoyama M, Mylonas E, Ohta N, Yagi N, Shinohara Y, Amemiya Y (2013) Hydrophobic molecules infiltrating into the poly(ethylene glycol) domain of the core/shell interface of a polymeric micelle: evidence obtained with anomalous small-angle X-ray scattering. *J Am Chem Soc* 135:2574–2582